Estimations of ocean stratification and sea ice rafting: Key factors in recent sea ice variations in the Arctic Ocean

メタデータ	言語: eng 出版者: 公開日: 2016-07-04 キーワード (Ja): キーワード (En): 作成者: 吉澤, 枝里 メールアドレス: 所属:
URL	https://oacis.repo.nii.ac.jp/records/1302

Doctoral Dissertation

ESTIMATIONS OF OCEAN STRATIFICATION AND SEA ICE RAFTING: KEY FACTORS IN RECENT SEA ICE VARIATIONS IN THE ARCTIC OCEAN

March 2016

Graduate School of Marine Science and Technology
Tokyo University of Marine Science and Technology
Doctoral Course of Applied Marine Environmental Studies

Eri Yoshizawa

Abstract

The Arctic sea ice cover in summer has shown a significant downward trend since the late 1990's, suggesting great influences on the global climate system. Furthermore, interests in commercial shipping using the Northern Sea Route have been rising due to the prolonged ice-free period observed especially in coastal regions of the Arctic Ocean. In order to assess both scientific and socio-economical impacts of the summer sea ice retreat, the accurate prediction of summer sea ice distributions is required. In the prediction of sea ice distributions, the sea ice thickness in spring is an important precondition of whether sea ice can survive or not during the following summer. Since the dominant sea ice type in the Arctic Ocean has been replaced from multi-year ice by first-year ice during the last decade, the sea ice thickness in spring mainly depends on sea ice growth during the preceding winter. In the present study, we focus on two key factors affecting the sea ice growth: thermal stratifications in the upper ocean and sea ice rafting due to convergent sea ice motions, and develop methods to estimate these factors using satellite-derived data.

-Estimation of upper ocean stratifications-

Thermodynamically, sea ice growth strongly depends on thermal stratifications in the upper ocean. In the Pacific sector of the Arctic Ocean where the maximum sea ice retreat has been observed, the warm Pacific Summer Water (PSW) lying just beneath the surface mixed layer is a major heat source affecting the sea ice cover. PSW is delivered from the shelf region to the basin by the upper ocean circulation in the Canada Basin, called as "the oceanic Beaufort Gyre (OBG)". Thus, the volume transport of the OBG is a reasonable indicator of the thermal state of the upper ocean.

Spatial distributions of ocean dynamic height (ODH) in the last decade showed that the center of the OBG was always located in the area just east of the Northwind

Ridge. Additionally, the ODH values in the eastern rim of the gyre have not shown inter-annual variations since the early 2000s. Since the volume transport is proportional to the difference in the ODH values between the center and rim of the gyre, we can use the value of ODH near the stable center as a proxy of the volume transport (hereafter referred to as ODH_{center}). Observational evidences also showed that the spatial pattern of the OBG did not correspond to that of the overlying sea ice gyre, suggesting there was a time lag of the OBG response relative to the surface forcing. The nature of such an oceanic inertia enables us to forecast the thermal state in the upper ocean within the time scale of the delayed oceanic response. Based on the Sverdrup relation, we attempt to estimate the volume transport of the OBG from surface forcing data.

Using multiple regression models that evaluated relative contributions of past surface forcing to the current state of the OBG, the time scale of the delayed response of the OBG relative to the surface forcing was examined. As a result, the time scale of the delayed oceanic response was estimated to be about three years. The multiple regression models reflecting the estimated time scale successfully reconstructed the observed temporal variations of ODH_{center} in 2006-2012 from surface forcing data. The accuracy of the model using satellite-derived sea ice velocities was about 0.2 dynamic cm corresponding to about 2 % of the amplitude of the observed variations. This suggests that the volume transport of the OBG can be monitored without in-situ hydrographic observations.

-Estimation of sea ice rafting-

Sea ice rafting caused by convergence of sea ice motions is another key factor to increase sea ice thickness mechanically. In recent years, the zonal ice band formed by rafted sea ice has often remained through summer in the southern Canada Basin, the Chukchi Sea and the East Siberian Sea, known as choke-points of the Northern Sea

Route. Here, we present a method to estimate effects of sea ice rafting caused by convergent sea ice motions using the AMSR-E and AMSR2 derived data, and examine its spatial distributions in spring.

In order to evaluate sea ice rafting, we adopt a Lagrangian tracking method using satellite-derived sea ice motion data. Without thermodynamic sea ice growth, a reduction of sea ice area due to convergence of sea ice motions induces an increase in sea ice thickness and a resultant increase in sea ice concentration per unit area. Based on this relationship, we assume that sea ice rafting contributing to mechanical sea ice growth occurs when the following two conditions are satisfied: (1) a sea ice concentration after about one day (A_F) exceeds 100% due to the convergence of sea ice motions, (2) a proxy of sea ice type falls below the threshold. The second condition enables us to ignore effects of rafting of grease ice which does not contribute to sea ice growth. As a first step to evaluate influences of mechanical sea ice growth on summer sea ice variations, we assume that the integrated values of ($A_F - 100$) % along sea ice trajectories calculated from 1 November to 1 May as a proxy of sea ice rafting due to the convergence of sea ice motions (hereafter referred to as "effective convergence [*EC*]").

As a result, sea ice with large *EC* on 1 May was found in choke-point regions of the Northern Sea Route. Especially, in these regions, the values of the correlation coefficient between *EC* on 1 May and sea ice concentration in the following summer from July to September were >0.58, which were significant at 90 % confidence level. The results showed that sea ice rafting caused by convergent sea ice motions during winter was critical to summer sea ice variations, and suggest summer sea ice distributions in choke-point regions can be forecasted several months ahead of summer using satellite-derived data.

Acknowledgements

I would like to express my sincere gratitude to Dr. Koji Shimada for his fruitful suggestions, thoughtfulness, and persistent coaching. I also appreciate his providing me valuable opportunities to participate in the Arctic expeditions. I am indebted to Prof. Jiro Yoshida and Dr. Fumiaki Kobashi for their fruitful comments. I greatly appreciate the efforts of Takashi Kamoshida in developing the sea ice motion data set. I am deeply grateful my appreciation to Prof. Kyung-Ho Chung, Prof. Sung-Ho Kang, Dr. Ho-Kyung Ha and Dr. Tae-Wang Kim for their valuable suggestions and kind cooperation. Finally, I also thank all the members and ex-members of our laboratory.

Contents

1. General introduction

Temporal and spatial variations of the Arctic sea ice have been monitored by satellite measurements since 1978 in the Arctic Ocean (Fig. 1a). The annual minimum of sea ice area (SIA) observed in September has shown a downward trend, with rapid reduction events in 1989–1990, 1998, 2007, and 2012 (dashed curve in Fig. 2a). Especially, the downward trend from 1998 to 2007 was enhanced, -10.7 ± 0.8%/decade, compared to that from 1979 to 1998, -3.0 ± 0.4%/decade (Comiso 2008). After 2007, SIA in September did not rebound to any levels observed prior to 2007, even though there were slight recoveries in 2008 and 2009 (Fig. 2a). In 2012, eventually, SIA in the entire Arctic Ocean hit the record minimum. According to predicted results from models participating in Intergovernmental Panel on Climate Change (IPCC), the Arctic Ocean will be a completely ice-free condition in summer by the end of this century (Holland et al., 2006; Stroeve et al., 2007).

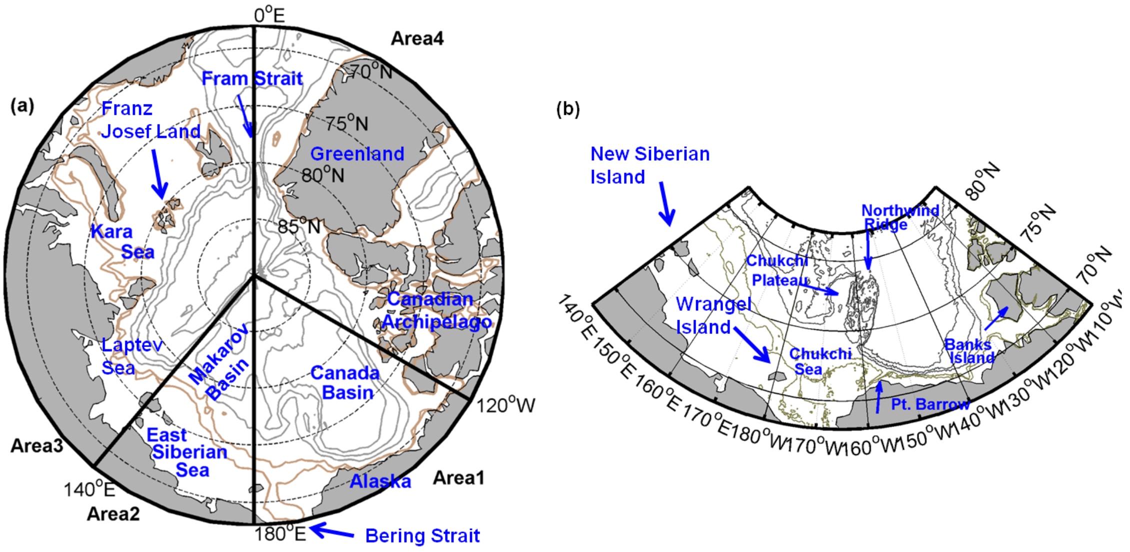

Figure 1 Study area with bottom topographies. **a** The Arctic Ocean, **b** the Pacific sector of the Arctic Ocean. *Grey solid contours* indicate seafloor topographies deeper than 1000m, contour interval 1000m. *Brown contours* denote 50 and 100 m isobaths.

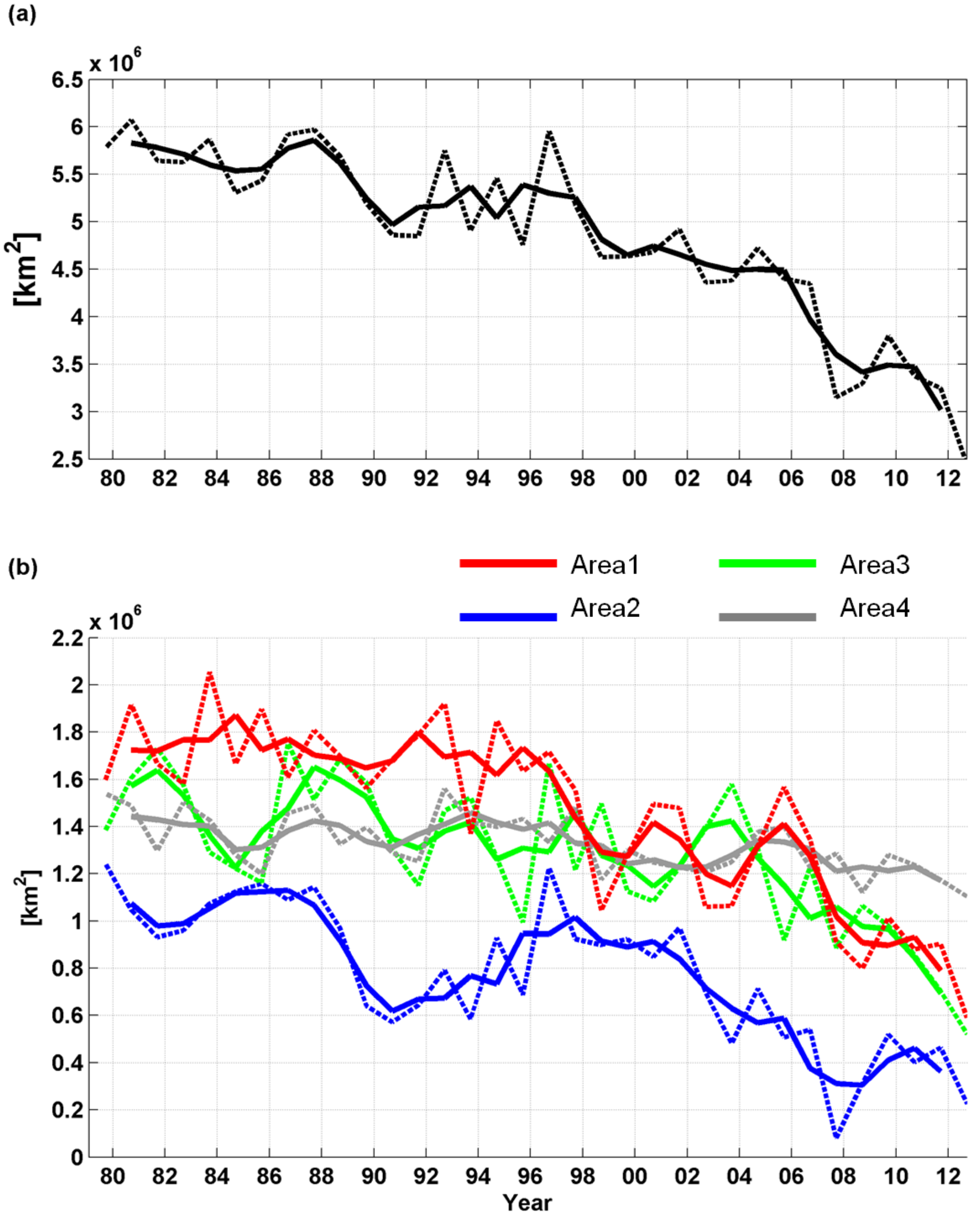

Figure 2 Time series of SIA (km^2) in September **a** in the entire Arctic Ocean, the area north of 68°N, **b** in the individual four areas depicted in Fig. 1a; Area 1 (120-180°W, *red curve*), Area 2 (140-180°E, *blue curve*), Area 3 (0-140°E, *green curve*), Area 4 (0-120°W, *grey curve*) measured by SSMR, SSM/I and SSMIS sensors. *Thick* and *thin curves* denote three-year running mean values and annual values, respectively.

The warming of surface temperature from 1901 to 2012 was most evident in the Arctic Ocean due to the extreme sea ice loss in recent decades, suggesting great impacts on the global climate system (Jones et al., 2014). For example, the less sea ice condition in the Arctic Ocean modulated the climate system in the mid-latitude region by anomalous heat fluxes from the open water surface to the overlying atmosphere (Fransis et al., 2009; Honda et al., 2009). Furthermore, with the shrinking of the summer sea ice cover, the length of the melt season was prolonged +1week/decade in 1979-2007, especially in Arctic coastal regions such as the Chukchi, Beaufort, East Siberian and Laptev Seas (Markus et al., 2009). It is predicted that the length of the ice-free period in the end of this century will double from that in the last century in both Northwest and Northeast passages of the Northern Sea Route (NSR) (Kohn et al., 2010).

To evaluate influences of the recent sea ice retreat not only on the global climate change but also on the utilization of the NSR, the accurate prediction of sea ice distributions is needed. In recent years, the retreat of the summer sea ice cover has been larger in the Pacific sector than that in elsewhere in the Arctic Ocean (Kwok et al., 2009). However, the numerical results from the IPCC prediction models showed that the Arctic ice cover equivalently retreated northward in both Pacific and Atlantic sectors, except the area north of the Greenland (e.g., blue curve in Fig. 1b of Holland et al., 2006). The predicted sea ice distribution from the empirical prediction model also showed spatial discrepancies with the observed one. For example, the observed zonal sea ice band extended from the southern Canada Basin to the Chukchi Sea in the 2015 summer (background color in Fig. 3) did not be reproduced by the empirical prediction model introduced by Kimura et al. (2013) (green colored shading in Fig. 3). These spatial inconsistencies suggest that prediction models do not sufficiently take into account dominant processes controlling recent sea ice variations. Hence, in order to improve performance of predictions of sea ice distributions, it is fundamentally required to identify key factors in the mechanism of recent sea ice variations, based on observational data.

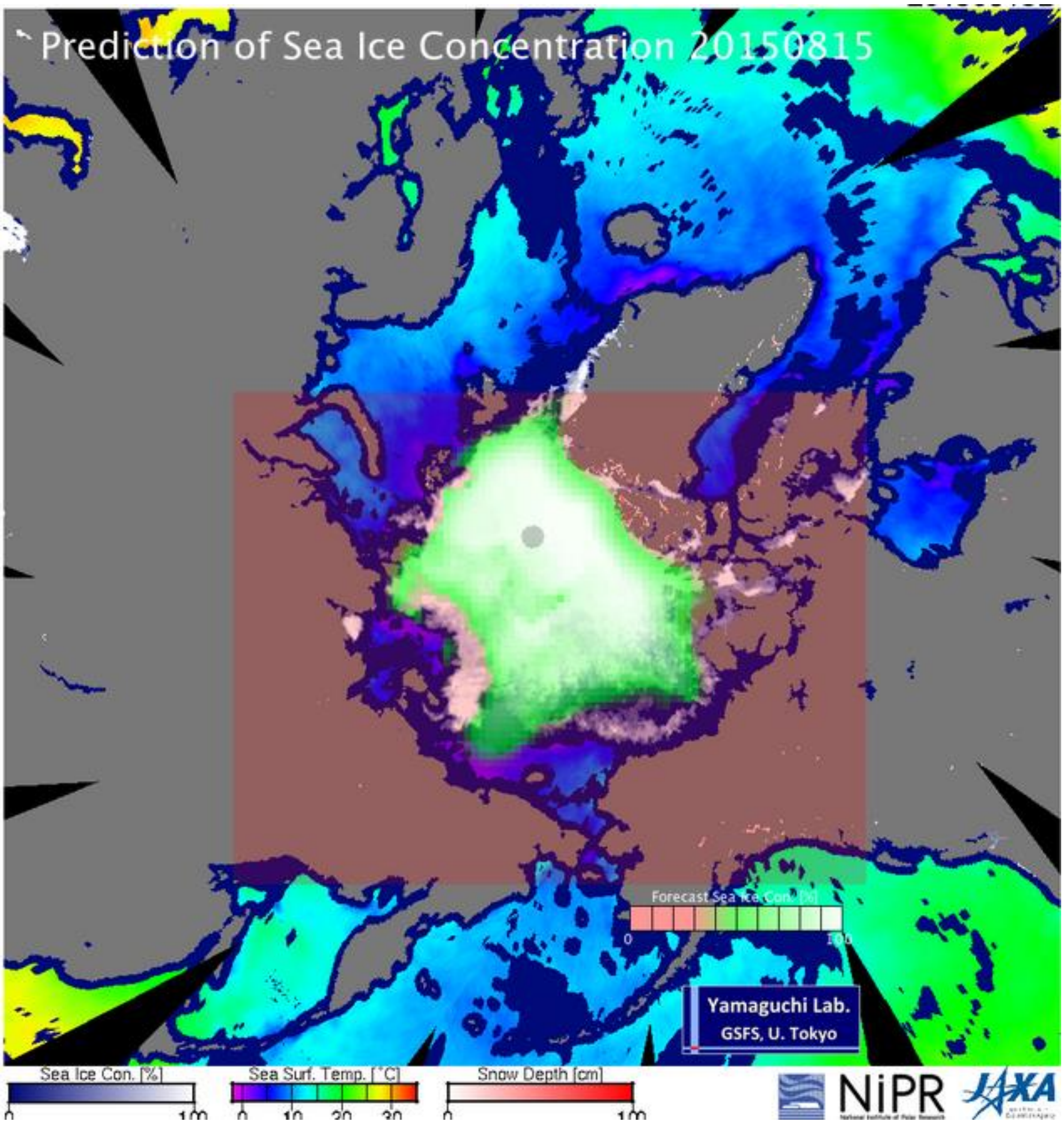

Figure 3 Spatial distributions of the observed sea ice concentration (*background color*) and of the predicted one (*green colored shading*) from the empirical prediction model presented by Kimura et al. (2013) on 15 August 2015 obtained at https://ads.nipr.ac.jp/vishop/vishop-monitor.html.

Sea ice thickness in spring is an important precondition of whether sea ice can be retained or not during the following summer. With the shrinking of the summer sea ice cover, the dominant sea ice type in the Arctic Ocean has been displaced from multiyear ice (MYI) by first year ice (FYI) (Maslanik et al., 2011; Comiso 2011; Polyakov et al., 2012). In this situation, the sea ice thickness in spring strongly depend on sea ice growth during the preceding winter. In the present study, we focus on following two factors affecting the sea ice growth: thermal stratifications in the upper ocean and sea ice rafting caused by convergent sea ice motions via rafting processes. Because of the limited availability of in-situ hydrographic and thickness data in the Arctic Ocean, we develop methods to estimate these two factors using satellite-derived data. This study is organized as follows. In Sect. 2, the relationship between surface forcing and ocean stratifications are examined. Based on observational results, an estimation method of ocean stratifications is presented. In Sect. 3, a method evaluating effects of sea ice rafting caused by the convergence of sea ice motions is developed. Section 4 gives conclusions of this study.

2. Estimation of ocean stratifications

2.1 Introduction

In this section, we focus on thermodynamic sea ice growth depending on a thermal state in the upper ocean. In the Pacific sector where the maximum sea ice retreat in the Arctic Ocean has been observed, Pacific Summer Water (PSW) lying just beneath the surface mixed layer is a primary heat source to affect the sea ice cover. Since PSW is transported to the basin by the upper ocean circulation (the oceanic Beaufort Gyre: hereafter referred to as the OBG), ocean stratifications in the OBG region is a key factor to quantify horizontal heat transports originating in PSW.

There is a direct way to estimate ocean stratifications from spatial distributions of sea surface height measured by satellite-installed altimeters, based on the geostrophic balance. However, the amplitude of the temporal variations of ocean stratifications, i.e., ocean dynamic height (ODH), was up to about 10 dynamic cm for the past decade (shown later in Sect. 2.4.2), which was not large enough to be detected by the accuracy of the altimeter data (~15 cm) (Kwok and Morison 2011). Therefore, we adopt a different approach based on the Sverdrup relation to evaluate variations of ocean stratifications, in which oceanic velocities are calculated by vorticity inputs at the sea surface.

In the case of the upper ocean circulation driven by only the Ekman pumping induced by a surface torque without any wave propagations and lateral vorticity inputs, the upper ocean circulation simultaneously responds to surface forcing (Proshutinsky et al., 2002). The observational evidence, however, showed that the spatial pattern of the OBG did not correspond to that of the overlying sea ice gyre (we will refer to this later in Sect. 2.4.2). The observed spatial inconsistency suggests that there was a time lag in the response of the OBG relative to surface forcing. Therefore, the time scale of this delayed oceanic response significantly influences oceanic heat transports into the basin and the resulting sea ice variations. As a first step to quantify influences of subsurface ocean heats on sea ice variations, we examine relative contributions of past surface forcing to the current state of the OBG. Based on the quantitative result, the thermal state of the upper ocean in the OBG region can be forecasted within a time scale that is shorter than the delayed oceanic response.

This section is organized as follows. The data description is given in Sect. 2.2. In Sect. 2.3, features of recent sea ice retreat are firstly reviewed, in order to introduce an importance of oceanic influences on summer sea ice variations. In Sect. 2.4, relationships among observed temporal variations of surface forcing, the upper ocean circulation and SIA are examined. The delayed oceanic response is recognized as a key to understanding actual variations of the summer sea ice cover in the OBG region. In Sect. 2.5, based on the observational results, we develop quantitative examinations of the delayed time scale of the OBG using a multiple regression analysis, and provide a simple model to forecast the state of the OBG. Finally, we give a summary of the section in Sect. 2.6.

2.2 Data description

We use hydrographic data collected under the Joint Western Arctic Climate Studies (JWACS) with CCGS LSSL 2002– 2008 (obtained at http://www.whoi.edu/beaufortgyre) and R/V Mirai 2002, 2004, and 2008 (obtained at http://www.godac.jamstec.go.jp/darwin/cruise/mirai), and under the Korea-Polar Ocean in rapid transition (K-PORT) expedition with the Korean icebreaker ARAON 2011 and 2012. We also use data from XCTD data stations, collected during CCGS LSSL 2009–2012, partly supported by Japan Aerospace Exploration Agency (JAXA) research projects [the International Arctic Research Center (IARC)-JAXA Information System, and the Global Change Observation Mission-Water (GCOM-W)].

We analyze sea ice motion data calculated by the maximum cross correlation method, the so-called particle image velocimetry (PIV) method (e.g., Adrian 1991), for brightness temperature images obtained from the Advanced Microwave Scanning Radiometer for Earth observing system (AMSR-E) (Kamoshida and Shimada 2010). 89 GHz channel data gridded onto a polar-stereo projection (2.08 × 2.08 km) is mainly used. In their calculation, the first three correlation peaks are candidates for the calculation of sea ice velocity vectors. If the direction of the re-analysis 10 m wind is out of the range of ±60° relative to the estimated sea ice vector, the estimated value is judged as an unrealistic vector. They use 10 m wind data provided by the National Center for Environmental Prediction/National Center for Atmospheric Research (NCEP/NCAR) reanalysis (Kalnay et al., 1996), obtained at http://www.esrl.noaa.gov/psd/. The accuracy of their daily sea ice velocities was evaluated by comparison with other sea ice motion data measured by the bottom-tracking mode of upward-looking acoustic Doppler current profilers (ADCPs), mounted on subsurface moorings that were located in the Chukchi Borderland area. The root mean square of the difference between the satellite-derived velocities and the actual measured ones by ADCPs was 2.5 cm s^{-1} during November 2002 to April 2003. Here, we analyze sea ice velocities averaged from November to June. The accuracy of the averaged velocity is much better than that of the daily one, and is accurate enough to estimate the temporal variations of ODH in the OBG region. For the period in which AMSR-E was not operated, sea ice motions are calculated using brightness temperature images obtained from the following sensors: Scanning Multichannel Microwave Radiometer (SMMR) and Special sensor Microwave/Imager (SSM/I). Operation periods of these sensors are listed in Table 1.

We use sea ice concentration data derived from the National Aeronautics and Space Administration (NASA) team algorithm (Markus and Cavalieri 2000), provided by the National Snow and Ice Data Center (NSIDC).

Table 1. Operation periods of passive microwave sensors.

sensor	SMMR	SSM/I	SSMIS	AMSR-E	AMSR2
period	1978/10 -1987/08	1987/08 -2009/04	2009/04 -present	2002/06 -2011/09	2012/06 -present

2.3 Features of recent sea ice retreat

As we mentioned in Sect. 1, the temporal variations of the September SIA has shown the significant downward trend with the anomalous reductions in 1989–1990, 1998, 2007, and 2012 (dashed curve in Fig. 2a). In order to investigate whether these reductions occurred in the entire Arctic Ocean or were dominated by specific regions, time series of SIA in September in the four distinct areas (areas 1–4 in Fig. 1a) are shown in Fig. 2b. The rapid reduction in 1989–1990 was led by the reduction in the eastern hemisphere in the Arctic Ocean (areas 2 and 3), where the sea ice motion is characterized by the Transpolar Drift Stream (TDS) of sea ice (blue and green curves in Fig. 2b). The reduction in this region is interpreted as discharges of sea ice from the Arctic Ocean to the Greenland Sea through the Fram Strait. The discharge correlates with variations of climatic indices such as the Arctic Oscillation (AO) that was firstly defined by Thompson and Wallace (1998) as a first empirical orthogonal function (EOF) mode of sea level pressure (SLP) in the area north of 20^{o}N. Rigor et al. (2002) showed that the positive AO anomaly in winter related to the decline of sea ice extent in the following summer during 1979 to 1998. In 1989-1990, in contrast, no significant change was observed in the western hemisphere (areas 1 and 4) (red and grey curves in Fig. 2b). The second rapid reduction in 1998 was led by the regional reduction in the Canada Basin (area 1) (red curve in Fig. 2b), without significant changes in other areas (blue, green, and grey curves in Fig. 2b). These regional contrasts suggest that the mechanism of sea ice reduction differs from region to region.

During 1998 to 2007, the SIA reduction trends in areas 1, 2, and 3 were much larger than those before 1998 (red, blue and green curves in Fig. 2b). In this period, the AO index in winter was neutral or negative, and it did not correlate with the SIA variations (Shimada et al., 2006). Based on numerical results, Watanabe et al. (2006) showed that the positive (negative) Dipole Anomaly (DA), which was defined as a second EOF mode of SLP in the area north of 70°N, increased (decreased) the sea ice outflow through the Fram Strait. Although the positive DA anomaly correlated with anomalous record lows of the summer SIA in 2005 and 2007, it did not explain the enhanced downward trend of SIA after 1998 (Wang et al., 2009). SIA in areas 1, 2, and 3 hit the record minimum in 2012, even though there were slight recoveries of SIA were observed after 2007 (red, blue and green curves in Fig. 2b).

Figure 4 shows spatial patterns of ice edge (15 % sea ice concentration) in September during 1979–1997, 1998–2006, and 2007–2012. Grey dashed contours are 500 m isobaths on the continental shelf slopes. During 1979–1997, before the rapid SIA reduction in 1998, open water areas were found only in the shallow shelf regions (black chained curve in Fig. 4). During 1998–2006, before the anomalous sea ice reduction in 2007, an embayment-shaped sea ice retreat into the basin was observed in the western Canada Basin (black dashed curve in Fig. 4). In other areas, the ice edges were still located in the shelf regions or on the shelf slopes. During 2007–2012, in the East Siberian and Kara Seas, the ice edges moved offshore but did not enter into the basin deeper than 500 m (black solid curve in Fig. 4). In the Canada Basin, however, the open water area was enlarged northward along the Northwind Ridge and the Chukchi Plateau (Fig. 1b), where the major pathway of PSW was identified (Shimada et al., 2001; Steele et al., 2004). In this area, the significant downward trend of the summer sea ice concentration at 90 % confidence level was also found in 2000s (color in Fig. 5). These spatial consistencies suggests that the oceanic heat is a key component to understanding the regional sea ice change in the Pacific sector of the Arctic Ocean showing the significant downward trend of the summer SIA after the late 1990s (red curve in Fig. 2b).

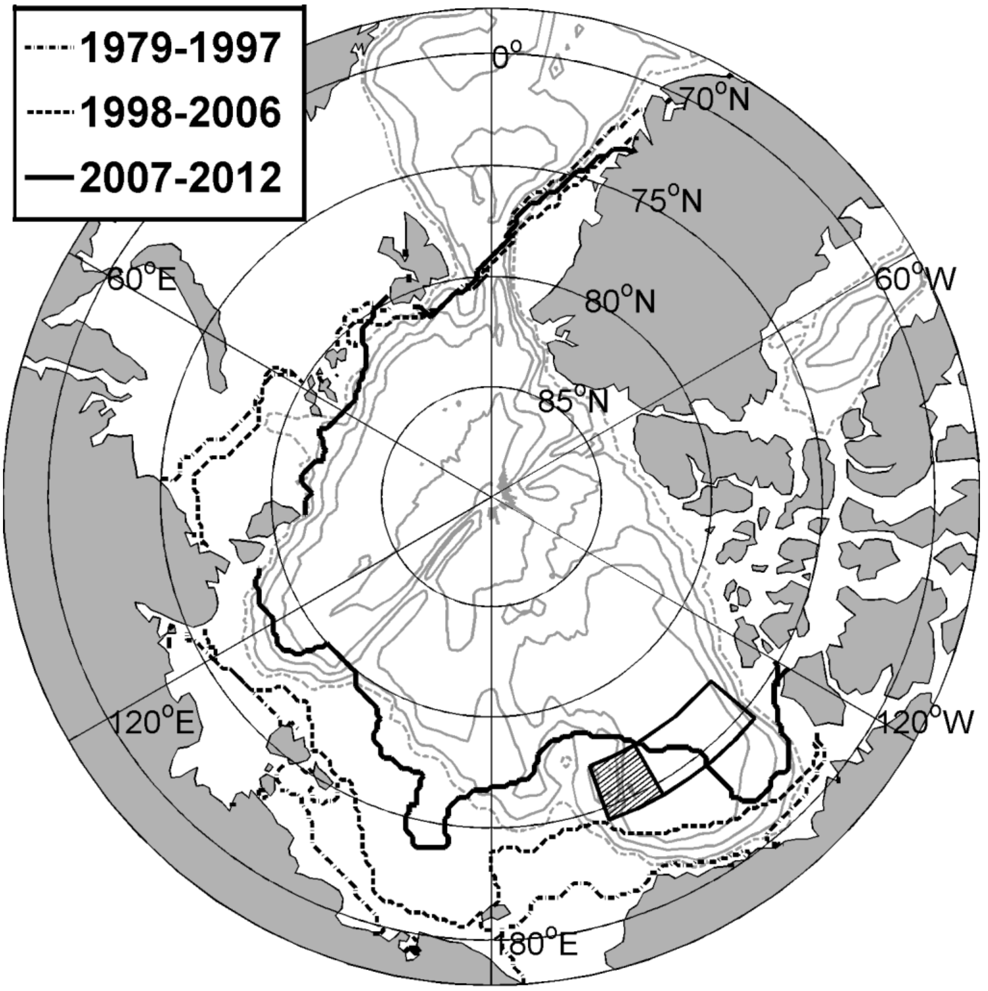

Figure 4 Spatial patterns of ice edge (*contours* of 15% sea ice concentration) in September averaged for the following three periods; 1979-1997 (*black chained curve*), 1998-2006 (*black dashed curve*), 2007-2012 (*black solid curve*). *Grey solid contours* indicate seafloor topographies deeper than 1000m, contour interval 1000m. *Grey dashed contours* denote 500m isobaths. The *zonal band*, 74.4-77°N, 130-160°W, shows the area for which time series of curls of NCEP 10 m wind velocities and of sea ice velocities shown in Fig. 6a and 6b were calculated. The *black hashed box*, 74.4-77°N, 150-160°W, is the area used to calculate time series of ODH_{center} shown in Fig. 6c.

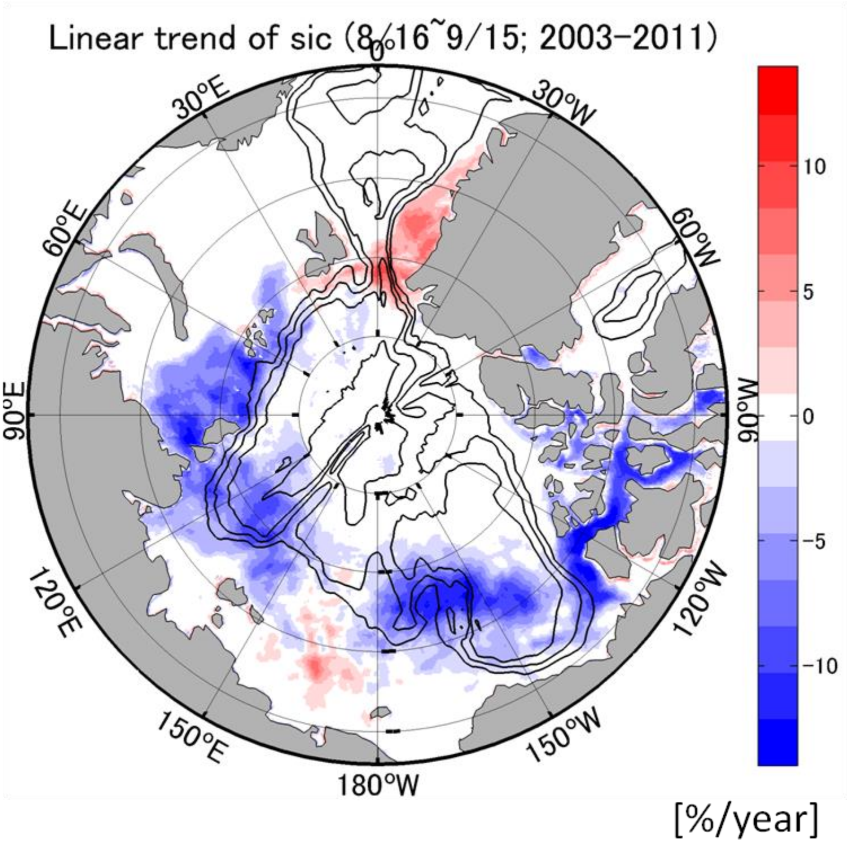

Figure 5 Linear trends of sea ice concentration from 16 August to 15 September of the AMSR-E period, 2003-2011 (*color*). Trends significant at 90 % confidence level by the two-tailed t test are shaded.

2.4 Relationship between surface forcing and ocean stratifications

To develop a method to estimate ocean stratifications in the OBG region, we examine relationships between the temporal variations of ocean stratifications and of driving forces of the OBG, such as winds and sea ice motions. Shimada et al. (2006) explained that the strengthening of the OBG was initiated in the late 1990s by the strengthening of the basin-scale sea ice motion due to less friction of the sea ice cover against the Alaskan Beaufort coast. Using hydrographic data from the late 1990s to the mid 2000s, they suggested that more oceanic heat leading to the substantial sea ice reduction was delivered to the western half of the OBG. Then, we also attempt to identify which parameters have controlled the observed temporal variations of the summer SIA, with a particular focus on the sea ice variations after 2007.

2.4.1 Changes in curls of winds and sea ice velocities

First of all, we briefly mention features of spatial distributions of the OBG, in order to introduce how we can evaluate the volume transport by surface forcing data. In the climatological mean field, the OBG showed a zonally asymmetric pattern, and its center was located in the area just east of the Northwind Ridge (see Fig. 3 of Shimada et al., 2001). This suggests that the wave dynamics in the presence of the finite amplitude seafloor topography is essential to understanding the zonally asymmetric spatial pattern of the OBG. Sumata and Shimada (2007) explained that the modal exchange from the traveling barotropic Rossby wave to the stagnated baroclinic mode occurred around the wall, due to small planetary β effects, the Northwind Ridge and the Chukchi Plateau, facing to east in the Canada Basin. The non-propagating baroclinic mode formed northward currents within the narrow zonal band over the Northwind Ridge and the Chukchi Plateau. Then, the horizontal shape of the OBG resulted in the zonally asymmetric pattern, just like the mid-latitude subtropical gyre. Such spatial patterns were also found in our hydrographic data analysis, while spatial patterns of the overlying sea ice gyre showed large inter-annual variations (we will argue this in detail in Sect. 2.4.2). Thus, based on the Sverdrup relation, the vertically averaged volume transport of the OBG would be given by just the surface torque.

In the general Sverdrup theory for the ocean with flat bottom topographies, the curl of surface forcing zonally integrated from the center of the gyre to the eastern boundary is proportional to the vertically-averaged current velocity of the southward interior flow of the clockwise gyre. In the actual Canada Basin, however, the surface forcing imposed on the sea surface in the southeastern portion of the basin does not contribute to formations of baroclinic ocean structures, because gradual seafloor topographies excite topographic baroclinic Rossby waves (see Appendix A). Therefore, the values of the surface forcing curl in the southeastern Canada Basin are excluded when the relationship between the OBG transport and the surface forcing are examined. We set the zonal band in which the surface forcing curls are averaged, as depicted in Fig. 4 (black zonal band).

Since the climatological Ekman vertical velocity was very weak during July to September (Yang 2006), the curls during that period are ignored in the present study. The curls in October were also neglected, because the sea ice condition in the Canada Basin in that month makes it difficult to quantify relative contributions of winds and sea ice motions to the formation of the OBG. Assuming that drag coefficients at atmosphere–ice and ice–ocean interfaces are constant in the ice-covered period (November-June), we introduce the zonal mean value of curls in this period as a proxy of the vertical averaged velocity in the ocean. Hereafter, we define the averaged curl from November 2011 to June 2012 as the curl in 2012.

Figure 6a and 6b show time series of curls of NCEP10 m winds and of satellite-derived sea ice velocities averaged for the ice-covered period from November to June in the zonal band depicted in Fig. 4, respectively. During 1979–1996, the wind curl increased (Fig.6a), while there were no significant changes in both the sea ice velocity curl (Fig. 6b) and SIA in the Canada Basin (Fig. 6d). This suggests that vorticities of surface winds did not penetrate into sea ice under the heavy ice condition during this period (Shimada et al., 2006). From 1997 to 2004, the sea ice velocity curl decreased (Fig. 6b) coherently with a decrease in the wind curl (Fig. 6a). This suggests that the atmosphere-ice kinematic coupling was getting larger than that before 1997 (see Appendix B). When the anomalous summer sea ice reduction was observed in 2007–2008 (Fig. 6d), both the wind and sea ice velocity curls decreased substantially, i.e., clockwise rotations were strengthened (Figs. 6a, b).

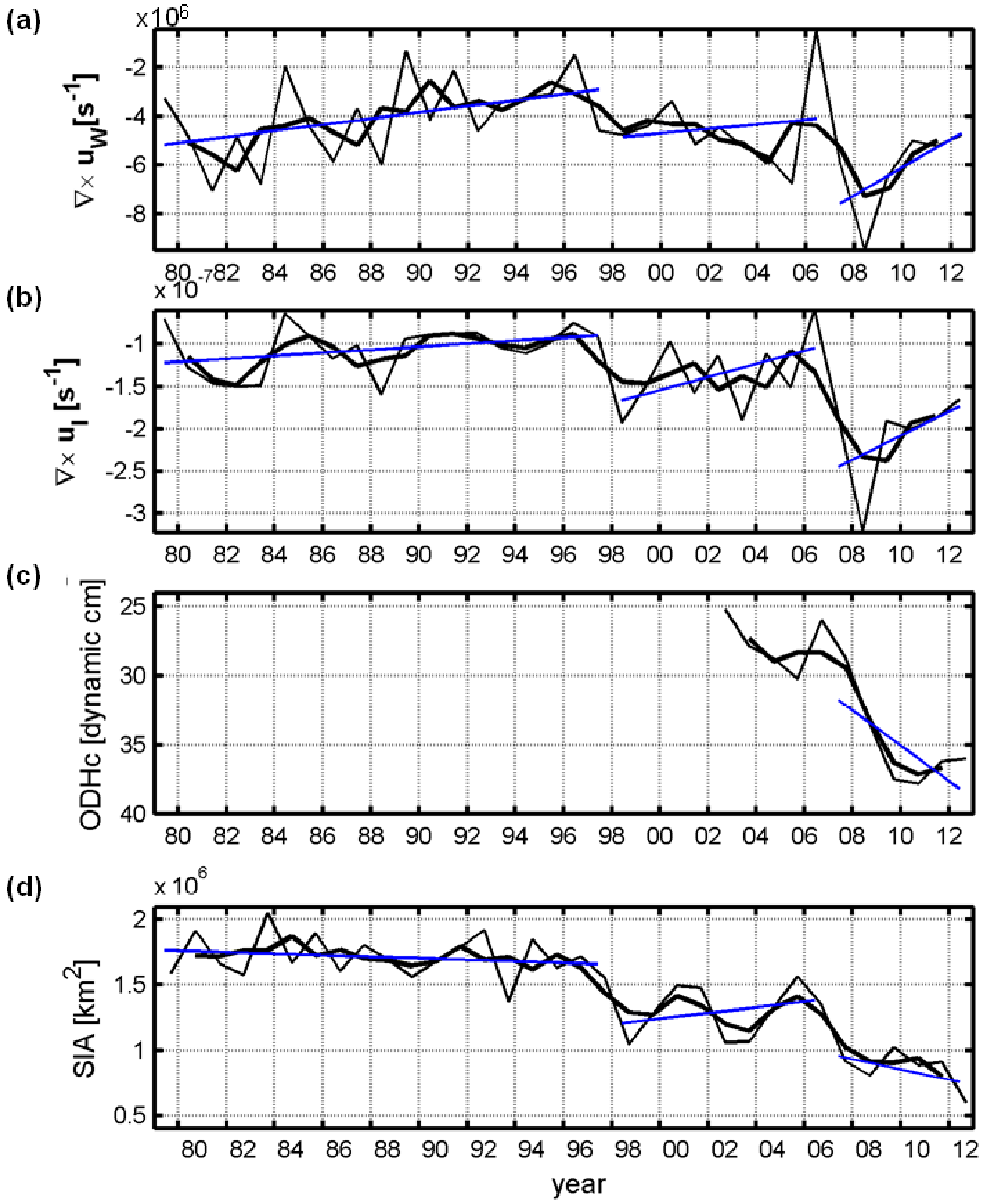

Figure 6 Time series of **a** spatial averages of the curl of NCEP 10 m wind velocities (s^{-1}) in ice-covered period (November-June) in the *black zonal band* depicted in Fig. 4, **b** the same as (a) but for the curl of sea ice velocities (s^{-1}), **c** spatial averages of ODH (dynamic cm) at 100 dbar relative to 800 dbar in summer (July-September) in the *black hashed box* depicted in Fig. 4, i.e., ODH_{center}, **d** SIA (km^2) in September in the Canada Basin (area 1 depicted in Fig. 1a). The z-axis in (c) is inverted. In (a)-(d), *thick* and *thin curves* denote three-year running mean values and annual values, respectively.

After 2009, the wind curl rebounded to the value observed around 2004 or in the mid 1980s (Fig. 6a). The sea ice velocity curl also rebounded after 2009, but the rebound did not reach the levels of the three-year running mean values before 2007 (Fig. 6b). Even though the curls rebounded, SIA in the Canada Basin continued to decrease after 2009 (Fig. 6d). This implies that the observed variations of SIA in the Canada Basin cannot be explained by just the surface forcing, and some oceanic delayed processes, i.e., “ocean inertia” effects, may be necessary to interpret the observed SIA variations after 2007–2008. Before we examine the delayed temporal response of the OBG to the surface forcing, we review recent variations of the OBG, as well as the heat content in the subsurface layer (25–150 m) in the western Canada Basin where the warm PSW is delivered.

2.4.2 Changes in the OBG and ocean heat content

PSW usually arrives at the southern portion of the Northwind Ridge around January and then spreads into the basin (Sumata and Shimada 2007). In-situ hydrographic observations covering the OBG region, however, have been temporally limited in summer. Hydrographic data of the zonal cross section of the northward flow of the OBG was obtained by subsurface ocean mooring systems from August 2011 to August 2012, and temporal variations of northward geostrophic velocities were calculated (not shown). The standard deviation of the northward geostrophic velocity was 0.28 cm s^{-1}, whereas the annual mean velocity was 1.64 cm s^{-1}. Since the seasonal variation of the northward geostrophic velocity was enough smaller than the annual mean, we can use the observed ocean stratification in summer as a representative of the year.

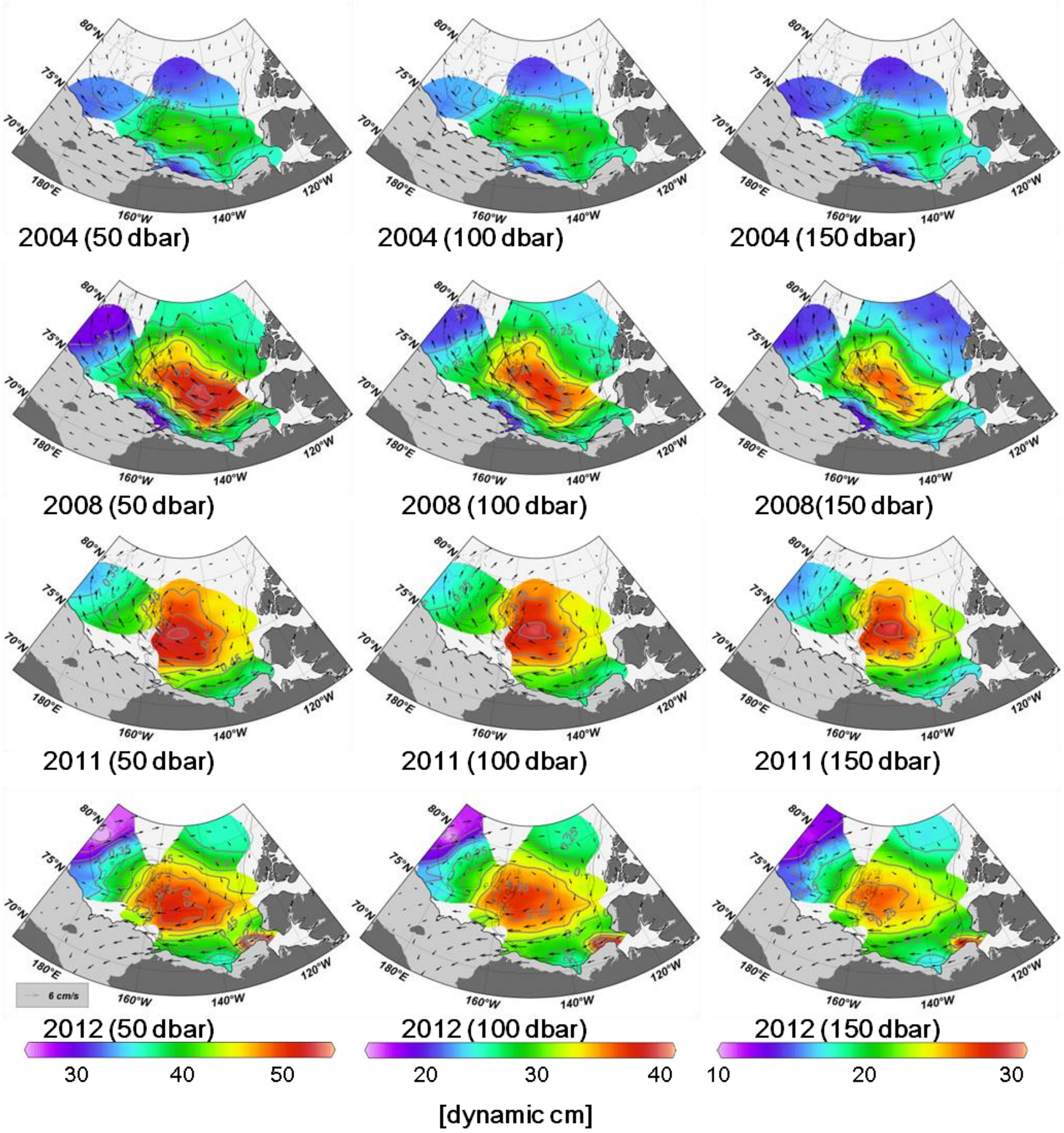
2004 (50 dbar) 2004 (100 dbar) 2004 (150 dbar)

2008 (50 dbar) 2008 (100 dbar) 2008(150 dbar)

2011 (50 dbar) 2011 (100 dbar) 2011 (150 dbar)

2012 (50 dbar) 2012 (100 dbar) 2012 (150 dbar)

Figure 7 Spatial distributions of ODH (*color*, dynamic cm) at 50, 100, and 150 dbar relative to 800 dbar in summer (July-September) of 2004, 2008, 2011, and 2012, and sea ice motions (*vector*, cm s^{-1}) in preceding ice-covered period (November-June).

Figure 7 shows spatial distributions of ODH relative to 800 dbar in the summers (July–September) of 2004, 2008, 2011, and 2012 at 50, 100, and 150 dbar (color). For these four summers, hydrographic observations covering both eastern and western portions of the OBG region are available. Sea ice motions in preceding ice-covered periods (November–June) are also overlaid as vectors. In the summers of 2004, 2011, and 2012, ODH showed patterns that were almost the same at the three levels (first, third and forth lines in Fig. 7). In the summer of 2008, however, the pattern of ODH at 50 dbar (left panel of second line in Fig. 7) slightly differed from the patterns at the deeper levels of 100 and 150 dbar (middle and right panels of second line in Fig. 7). The center of the OBG at 50 dbar in 2008 was not localized just east of the Northwind Ridge, but showed a zonally broad pattern extending southeastward, toward the Canadian Beaufort Sea. The freshwater inputs arising from the melting of MYI anomalously increased in the summers of 2007 and 2008 in the Canadian Beaufort Sea (Yamamoto-Kawai et al., 2009; Kwok and Cunningham 2010). These freshwater inputs would cause the broadening of the pattern of ODH at 50 dbar observed in the summer of 2008. In 2008, at deeper levels, the center of the OBG was observed at almost the same location, just east of the Northwind Ridge as in the other three years (middle and right columns in Fig. 7). The observational evidence suggests that the influence of the melt water inputs on the circulation pattern was small at levels deeper than 100 dbar. Therefore, the changes and distributions of ODH at these deeper levels would mainly be established by the dynamical response to the kinematic surface forcing.

At 100 and 150 dbar, northward currents in the zonally narrow area of the Northwind Ridge and the Chukchi Plateau were observed in all four years, while overlying sea ice motions were westward in these regions, i.e., sea ice velocity vectors were perpendicular to the direction of the oceanic geostrophic flows (middle and right columns in Fig. 7). Such discrepancies in the spatial patterns of the oceanic and sea ice gyres support the notion of a significant role of topographic features of the finite amplitude seafloor, the Northwind Ridge and the Chukchi Plateau, in the formation of the OBG, as pointed out by Sumata and Shimada (2007). In such cases, the difference in ODH values between the center and rim of the gyre is proportional to the volume transport, based on the Sverdrup relation. Turning to the eastern rim of the OBG, near the Banks Island in the Canadian Archipelago, the ODH values did not change significantly year to year at any of the three levels (Fig. 7). Hence, we can assume the ODH value near the stable center of the OBG as a proxy of the volume transport. Here, we define the spatial average of ODH in the black hashed box depicted in Fig. 4 as a proxy of the northward volume transport. This spatial average of ODH is hereafter referred to as ODH$_{center}$.

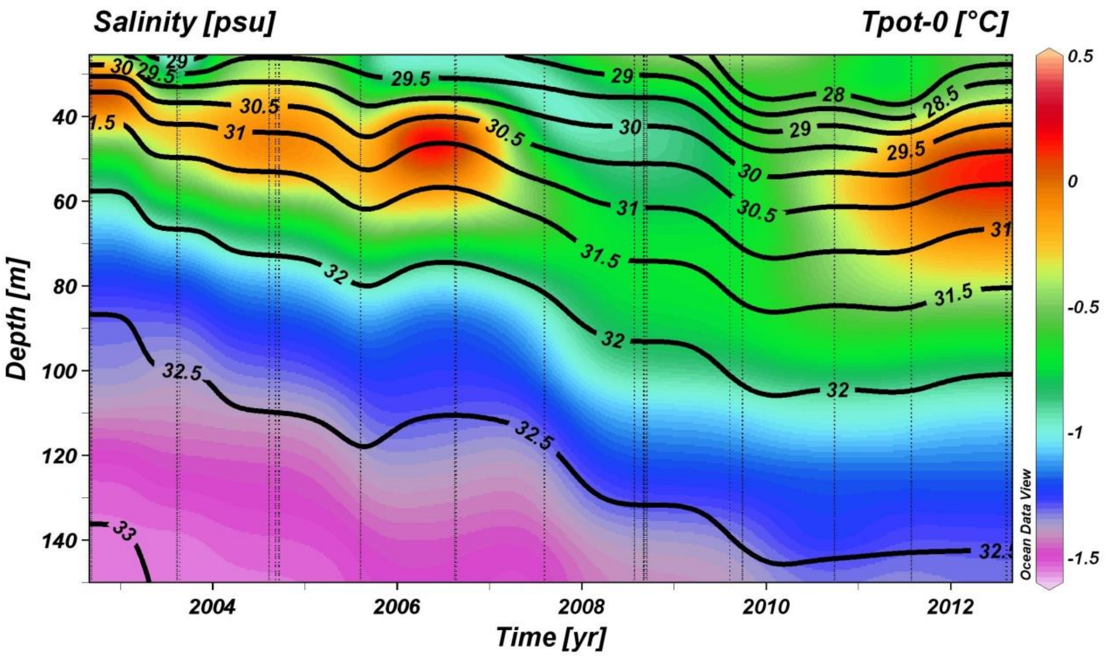

Figure 8 Time series of depth-averaged potential temperature (*color*, ^{o}C) and salinity (*black contours*), using spatially-averaged values in the region near the Northwind Ridge, the *black hased box* depicted in Fig. 4.

Figure 6c shows temporal variations of ODH_{center} at 100 dbar, which correspond to the lower level of the PSW layer, relative to 800 dbar. The *z*-axis in the figure was inverted. The annual value of ODH_{center} increased remarkably from 2007 to 2010 (thin curve in Fig. 6c). This shape was similar to those of the three-year averaged the wind and sea ice velocity curls and in 2006–2009 (thick curve in Figs. 6a, b), but ODH_{center} showed time lags of about two years relative to the curls. Trends of these observed variables in 2007–2012 indicate that both the loss of SIA (blue line in Fig. 6d) and the volume transport of the OBG (blue line in Fig. 6c) increased, while clockwise rotations of winds and sea ice motions decreased (blue line in Figs. 6a, b). This suggests that the OBG rather than the surface forcing has much more immediate impact on the changes in SIA.

Figure 8 shows time series of potential temperature and salinity near the Northwind Ridge. The thickness of the PSW layer ($29.5 < S < 32.5$; Steele et al., 2004), associated with the oceanic thermal condition affecting the overlying sea ice cover, increased from 2007 to 2010. The thickness was nearly unchanged after 2009, even when the negative vorticity inputs by surface forcing decreased after 2009 (Figs. 6a, b). This suggests that the delayed response of the OBG to surface forcing is a potential candidate for maintaining lateral heat fluxes to the basin. This delayed oceanic response enables us to forecast the upper ocean state from the surface forcing in past years. In the following section, we attempt to construct a simple practical model to estimate the northward volume transport of the OBG without any hydrographic data.

2.5 Estimations of ocean stratifications

2.5.1 Equation

To estimate the temporal variations of ocean stratifications in the upper ocean, which determines heat fluxes toward the basin, from surface forcing data, relative contributions of curls of winds and sea ice velocities in past years to ODH_{center} is examined. This quantitative examination enables us to estimate the time scale of the delayed response of the OBG to the surface forcing. For this purpose, we consider the following multiple regression model that reconstructs the temporal variations of ODH_{center} using the wind curl or the sea ice velocity curl,

$$y_r(n) = \sum_{m=0}^{N} A_m x(n-m) + B, \qquad m = 0, 1, ..., M, \quad (2.5.1)$$

where y_r is the reconstructed ODH_{center}, and x is the observed wind or sea ice velocity curls. For example, to reconstruct ODH_{center} in the year n using the sea ice velocity curl, the curls in years n-0, n-1, ..., n-m are substituted into Eq. (2.5.1), where m is the time lag between the curl and ODH_{center}. The maximum time lag M is chosen arbitrarily. If we choose M=2, Eq. (2.5.1) is constructed from the sea ice velocity curl in years n-0, n-1, n-0, n-2. Eq. (2.5.1) in this case is hereafter referred to as "the model with the sea ice velocity curl for M =2".

In this study, ODH_{center} averaged from July of the year n to September of the year n is defined as " ODH_{center} in the year n", e.g., ODH_{center} averaged from July 2006 to September 2006 is defined as " ODH_{center} in 2006". On the other hand, the sea ice velocity curl averaged from November of the year n-1 to June of the year n, i.e., averaged for the ice-covered period of the year n, is defined as "the sea ice velocity curl in the year n", e.g., the sea ice velocity curl averaged from November 2005 to June 2006 is defined as "the sea ice velocity curl in 2006". Most of hydrographic data from which

ODH were calculated was taken in August in the year *n*, while the middle of the analysis period of the curl was 1 March in the year *n*. Then, the curl in the year *n* was originally preceded ODH$_{center}$ in the year *n* by about a half year. In Eq. (2.5.1), however, the time lag between them, *m*, is simply regarded as zero.

The relative contribution of $x(n\text{-}m)$ to $y_r(n)$ is statistically measured by the regression coefficient A_m in Eq. (2.5.1). *B* is a constant. A_m and *B* are calculated by a least squares technique, so as to

$$\sum_{n}^{N}\left\{A_m x(n-m)+B-y(n)\right\}^2$$

is minimized, where y is the observed ODH$_{center}$. For the maximum time lag *M*, there are *M*+2 unknowns (*M* +1 units of A_m and *B*). These *M*+2 unknowns are calculated by following *M*+2 equations:

$$\sum_{n}^{N}\left\{A_m x(n-m)+B-y(n)\right\}=0,$$

$$\sum_{n}^{N}x(n-m)\left\{\sum_{m}^{N}A_m x(n-m)+B-y(n)\right\}=0, \quad m=0,\ 1,\ \ldots M,$$

where the second matrix consists of *M*+1 equations.

2.5.2 Time scale of response of the OBG to surface forcing

Before turning to the examination on relative contributions of the surface forcing in past years to the volume transport, we first reconstruct the temporal variations of ODH$_{center}$ in 2006-2012 using the model for *M*=0, i.e., the model with just the curl in the previous ice-covered period. As we have mentioned in Sect. 2.4.2, the response of the OBG showed the time lags relative to the surface forcing. The maximum value of the annual ODH$_{center}$ was observed in 2010 (thin curve in Fig. 6c), when both curls rebounded from the maximum negative value observed in 2008 (thin curves in Figs. 6a, b). Thus, we can expect that it is not appropriate to explain the volume transport by just the surface forcing in the previous ice-covered period. The variations of the reconstructed ODH$_{center}$ in 2006-2012 from the models for M=0 are shown in Fig. 9 (black dashed curve for the wind curl, black solid curve for the sea ice velocity curl), with that of the observed ODH$_{center}$ (red curve). Indeed, the models for M=0 did not reconstruct the realistic variations of ODH$_{center}$. To check the validity of models, the square of the correlation coefficient between the observed and reconstructed ODH$_{center}$ (referred to as r^2) and the root mean square of the difference between the observed and reconstructed ODH$_{center}$ (referred to as D) are listed in Table 2. r^2 quantifies the ratio of the observed variations explained by the model. The models for M=0 explain only about 20 % of the observed variations. In addition, D are 3.75 and 3.72 dynamic cm for the models with the wind curl and the sea ice velocity curl, which correspond to about 30 % of the amplitude of the observed variations in 2006-2012 (11.10 dynamic cm). The results suggest that the model should be constructed on the basis of the quantitative examination of the time scale of the delayed oceanic response.

Table 2. r^2 and D for models with the wind curl or with the sea ice velocities[a b].

Explanatory variable	wind curl		sea ice velocity curl	
Maximum time lag	M=0	M=4	M=0	M=4
r^2	0.207	0.982	0.221	0.998
D (dynamic cm)	3.75	0.561	3.72	0.180
The amplitude of the observed variations of ODH$_{center}$ in 2006-2012 (dynamic cm)		11.10		

[a] The square of the correlation coefficient between the observed and reconstructed ODH$_{center}$ in 2006-2012, r^2, is used to measure the ratio of the observed variations explained by the model.

[b] D is the root mean square of the difference between the observed and reconstructed ODH$_{center}$ in 2006-2012.

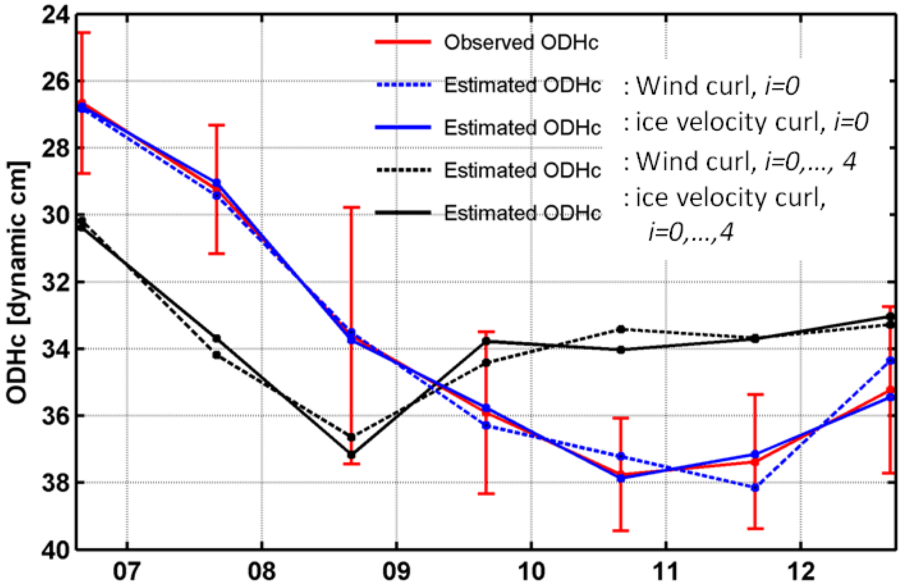

Figure 9 Time series of reconstructed ODH_{center} from the models for M=0 (*black curves*) and for M=4 (*blue curves*), with the observed ODH_{center} (*red curve*) (dynamic cm). Bars represent standard deviations of the observed ODH in the *black hashed box* depicted in Fig. 4 in each summer.

Next, using regression coefficients A_m, we attempt to examine relative contributions of the surface forcing in past years to the volume transport. A_m in models with the wind curl and the sea ice velocity curl for M=18 are shown in Fig. 10a and Fig. 10b, respectively (black curves). The amplitudes of A_m in both models are large for m=0, 1, 2, and decrease as m increases by m=4. Since the amplitudes of A_m drop to nearly zero at m=4, it seems reasonable to construct the models from curls at time lags m=0, 1, 2, 3, 4. The amplitudes of A_m, however, show a wavy-like oscillation for m>4. For example, A_m in the model with the sea ice velocity curl shows another peak at m=10 (black curve in Fig. 10b). Time series of the sea ice velocity curl showed rapid decreases in 1988, 1998, and 2008 (thin curve in Fig. 6b), suggesting that there was the step-like regime shift in the large-scale sea ice motion with intervals of ten years. Since A_m were calculated from such the temporal variations of the sea ice velocity curl with intervals of ten years, the partial peak of the amplitude of A_m would appear at $m = 10$.

Therefore, we here assume that the wavy-like variations of A_m for $m>4$ were appeared by artificial statistical influences. Consequently, we adopt the models for $M=4$ to reconstruct the variations of ODH$_{center}$.

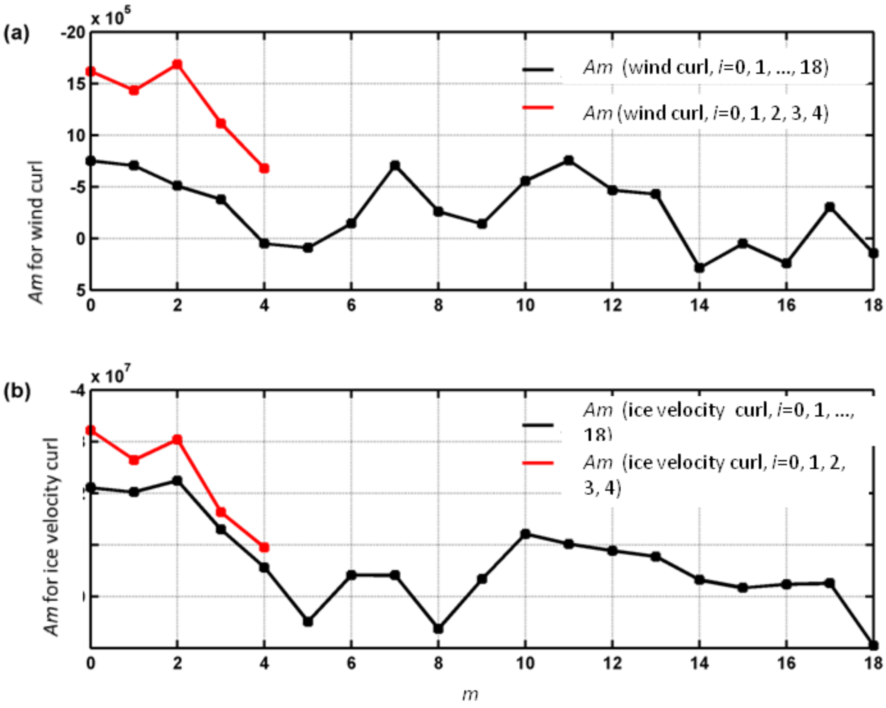

Figure 10 Regression coefficients A_m of the models with **a** the curl of NCEP 10 m wind velocities, **b** with the curl of sea ice velocities. The x-axis value m indicates the time lag between ODH$_{center}$ and the curl. *Black* and *red curves* denote A_m of the models for $M=18$ and $M=4$, respectively.

Table 3. Regression coefficients A_m in the multiple regression model, Eq. (2.5.1), constructed from the sea ice velocity curl at time lags $m=0$, 1, 2, 3, 4 (the maximum time lag $M=4$). [a]

Regression coefficients ($\times 10^8$)	A_0	A_1	A_2	A_3	A_4
	-0.322	-0.264	-0.304	-0.163	-0.094

[a] A_m represents a relative contribution of $x(n-m)$ to $y_r(n)$ in Eq. (2.5.1).

The reconstructed results from the models for M=4 are shown in Fig. 9 (blue dashed curve for the wind curl, blue solid curve for the sea ice velocity curl). The reconstructed variations showed good agreements with the observed ones depicted by red curve. The correlation coefficients between the observed and reconstructed ODH$_{center}$ are 0.991 for the wind curl and 0.999 for the sea ice velocity curl at the degree of freedom = 5, respectively (Table 2). Thus, the reconstructed results are statistically significant at more than 99 % confidence level. The models with the wind curl and the sea ice velocity curl for M=4 explain 98.2 and 99.8% of the observed variations, respectively. Moreover, D are 0.52 and 0.17 dynamic cm, i.e., about 5 and 2 % of the amplitude of the observed variations in 2006-2012, respectively. These agreements suggest that it would be adequate that we adopted the models constructed from the curls at time lags m=0, 1, 2, 3, 4.

A_m in the models for M=4 are shown in Fig. 10a for the wind curl and Fig. 10b for the sea ice velocity curl (red curves). The amplitudes of A_m in both models are relatively large for m=0, 1, 2, suggesting that the surface forcing in the past three ice-covered periods mainly contributed to the temporal variations of the volume transport (Table 3). Indeed, the models with the wind curl and the sea ice velocity curl for M=2 explain 60.0 and 85.7 % of the observed variations, respectively (not shown). Therefore, the time scale of the delayed response of the OBG to the surface forcing is estimated to be about three years.

Finally, we focus on the differences between the observed and reconstructed ODH$_{center}$ in the case using the models for M =4 (dashed curve for the wind curl, solid curve for the sea ice velocity curl in Fig. 11). There is the temporal increase in the differences in the case using the wind curl, while such a tendency is not seen in the case using the sea ice velocity curl. This would be due to changes in the strength in the kinematic coupling between winds and sea ice motions. Therefore, the more direct forcing data, the sea ice velocity curl, should be adopted for more precise evaluations of the upper ocean circulation.

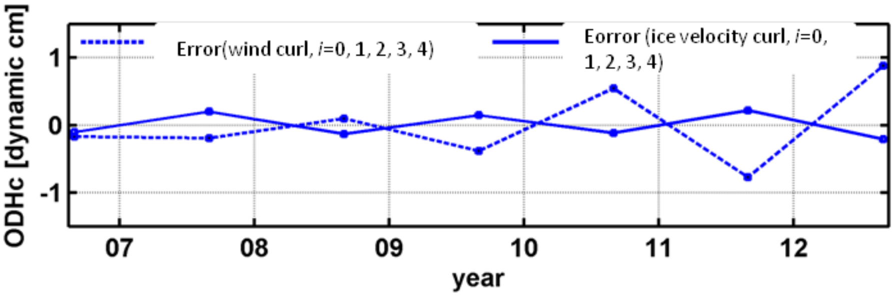

Figure 11 Differences between observed and reconstructed ODH$_{center}$ from the models for M=4. *Dashed* and *solid lines* denote errors of estimations from wind curls and from sea ice velocity curls, respectively.

2.6 Summary

The reinforced downward trend of the annual minimum of SIA since the late 1990s has been led by the anomalous sea ice reduction in the Pacific sector of the Arctic Ocean. In this region, the maximum sea ice retreat has been observed around the Northwind Ridge area where the warmest PSW distributed in the subsurface layer, suggesting that the subsurface oceanic heat is a key player of the anomalous sea ice reduction. In order to evaluate oceanic influences on summer sea ice variations, in this section, the method to estimate ocean stratifications that determine horizontal transports of the warm PSW to the basin was presented using surface forcing data.

Observational evidences showed that the location of the center of the OBG was stable, and there were no significant inter-annual variations in the ODH values in the eastern rim of the gyre. Thus, we used the ODH values in the stable center of the upper ocean circulation as a proxy of the volume transportation. The observed temporal variations of the volume transport lagged behind that of the zonal mean of the sea ice velocity curl, suggesting that there was the time lag of the OBG response relative to the surface forcing. Based on the multiple regression analysis between the volume transport and the sea ice velocity curl, the time scale of this delayed oceanic response was estimated to be about three years. Taking into account this quantitative result, the temporal variations of the volume transport in 2006-2012 were successfully reconstructed with high accuracies without in-situ hydrographic data.

3. Estimation of sea ice rafting

3.1 Introduction

In recent years, the Arctic coastal regions such as the southern Canada Basin, the Chukchi Sea, the East Siberian Sea and the Laptev Sea shown in Fig. 1a have been utilized as shipping routes. In these regions, the dominant sea ice type was replaced from MYI by FYI after the drastic sea ice reduction observed in the 2007 summer (Maslanik et al., 2011; Comiso 2011; Polyakov et al., 2012). It is expected that FYI melts out under the summer climate condition, however, sea ice often remained through summer locally in the Arctic coastal regions even in the FYI dominant condition. For example, sea ice like a tongue located around 72^{o}N in the East Siberian Sea remained through the 2010 summer (Fig. 12a). Recently, the zonal ice band was observed in the region from the southern Canada Basin to the Chukchi Sea even in the mid-summer of 2015 (Fig. 12b). The appearance of such robust sea ice in summer is key information for making a decision of whether or not the NSR is utilized for shipping.

In the prediction of summer sea ice distributions, sea ice thickness in spring is an important precondition of whether sea ice can survive or not during the following summer. In the FYI dominant condition, the sea ice thickness in spring mainly depends on sea ice growth during the preceding winter. In this section, we focus on mechanical sea ice growth caused by convergence of sea ice motions via rafting processes. The convergent field of sea ice motions is usually found in the southern Canada Basin, the

Chukchi Sea and the East Siberian Sea (color in Fig. 13), where robust sea ice remained through the summers (Fig. 12). Therefore, it is expected that convergent sea ice motions with rafting are associated with formations of robust sea ice.

Observations of sea ice thickness have been carried out by acoustic measurements (e.g., Rothrock 1999; Kwok and Rothrock 2009), but the coverage of data has been limited in time and space. In the lack of in-situ sea ice thickness data, Kimura et al. (2013) evaluate mechanical sea ice growth by the Lagrangian particle tracking method that particles uniformly arrayed on 1 December were tracked to 30 April using satellite-derived sea ice velocity data. They represented effects of mechanical sea ice growth during winter by the density of particles per unit area on 30 April. In their evaluation, convergent (divergent) sea ice motions increase (decrease) the density of particles per unit area, i.e., increase (decrease) sea ice thickness. However, in the actual Arctic Ocean, once convergent sea ice motions cause rafting of sea ice, the thickness of rafted ice does not decrease even under influences of divergent sea ice motions. In other words, sea ice does not act like a fluid. Therefore, in order to evaluate mechanical sea ice growth, influences of divergent sea ice motions that induce decreases in sea ice thickness should be excluded. In this study, we also adopt a Lagrangian tracking method using satellite-derived sea ice motion data, and attempt to develop the estimation method by taking into account such non fluid-like properties of sea ice. This section is organized as follows. In Sect. 3.2, data used here is described. In Sect. 3.3, a method to estimate effects of sea ice rafting caused by the convergence of sea ice motions is introduced. In Sect. 3.4, spatial distributions of the estimated sea ice rafting in the early May are examined, and the relationship of sea ice rafting with sea ice variations in the following summer from July to September is discussed.

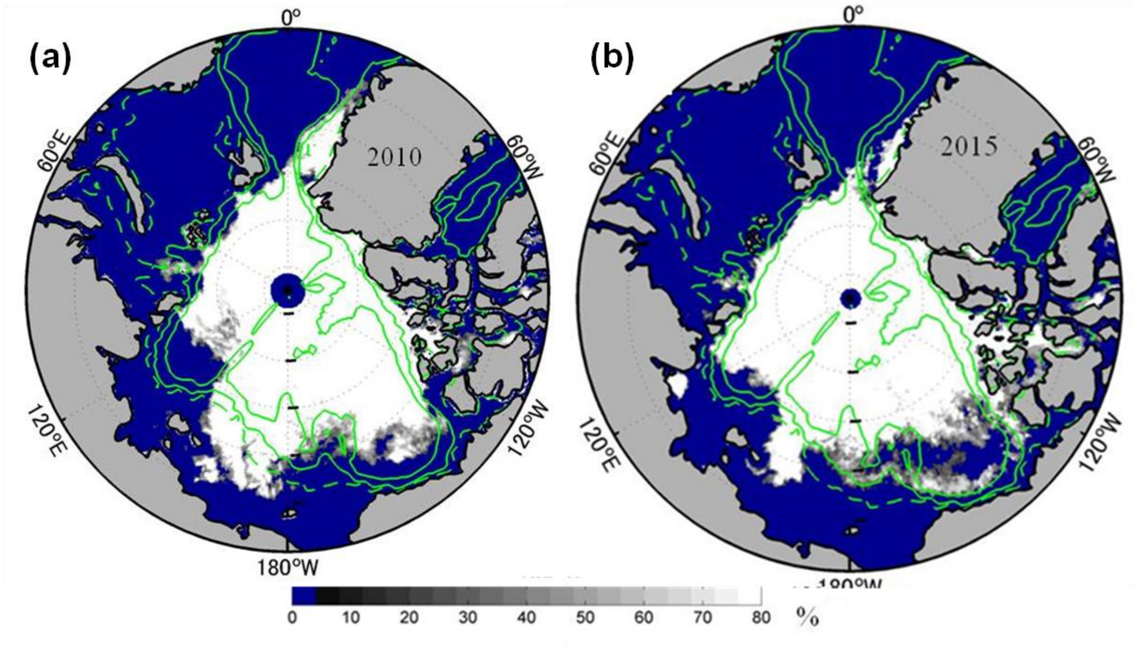

Figure 12 Spatial distributions of sea ice concentration [%] on 15 August **a** 2010 **b** 2015. *Green solid contours* indicate seafloor topographies deeper than 1000m, contour interval 1000m. *Green dashed contours* denote 500 m isobaths.

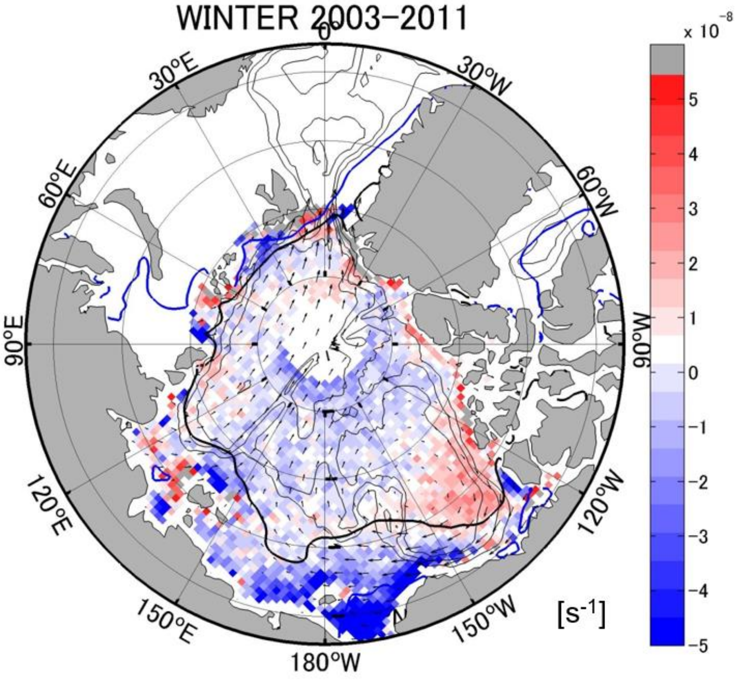

Figure 13 The spatial distribution of the divergence of sea ice velocities (*color*, s^{-1}) in the period from November to April of the AMSR-E period (2002-2011), with mean sea ice velocities (*vectors*, cm s^{-1}). The values are averaged at each grid cell in which sea ice velocities are defined.

3.2 Data description

We use data of brightness temperature (*Tb*), sea ice concentration (*A*) and timings of measurements (*Tm*) obtained from AMSR-E and AMSR2 measurements (obtained at https://gcom-w1.jaxa.jp/). The operation periods of these sensors are listed in Table 1. We also analyze daily averaged sea ice velocity data calculated from daily averaged brightness temperature images. The method to calculate sea ice velocities has been already described in Sect. 2.2. The time stamp of daily-averaged sea ice velocity data is defined as 00:00 of each day. Then, daily-averages of *Tb*, *A* and *Tm* are made here so that time stamps of these variables are adjusted to that of sea ice velocities.

3.3 Method

In this study, sea ice rafting is calculated along Lagrangian sea ice trajectories. First, sea ice trajectories are calculated backward from 1 May to 1 November of the preceding year using satellite-derived sea ice velocities. Since errors of these trajectories during November to April were smaller than that during May to October (see Appendix C), we focus on the period during November to April.

Next, we consider temporal variations of sea ice concentration caused by the convergence of sea ice motions at each grid in the polar-stereo coordinate, i.e., the Eulerian coordinate. Without thermodynamic sea ice growth, sea ice concentration after a time interval Δt is given by

$$A_F\,(t+\Delta t) = A(t) - \Delta t \times \left\{ A(t)\nabla\cdot\vec{u}\left(t+\frac{\Delta t}{2}\right)\right\}. \quad (3.3.1)$$

A_F is a forecasted sea ice concentration. A $(0 \le A \le 100\%)$ and $\vec{u}$ are observed sea ice concentration and horizontal sea ice velocity that were calculated using observed brightness temperature images, respectively. For example, at 81°N, 155°E (blue dot in Fig. 14), a measurement time on 7 October 2009 was 21:00 (Fig. 14a), while that on 8

October 2009 was 22:00 (Fig. 14b). Thus, Δt in Eq. (3.3.1) is given by the difference between timings of measurements at t and $t+\Delta t$. As a result of the calculation using Eq. (3.3.1), it is possible to be A_F >100%, if the large convergence of sea ice velocities occurs. In this study, we assume that sea ice rafting, which contributes to mechanical sea ice growth, is caused by convergent sea ice motions when A_F >100%. If sea ice thickness in the vicinity of the grid is homogeneous, a rate of a daily increase in the thickness can be represented by $R = (A_F - 100)$ %.

Once convergent sea ice motions cause rafting of sea ice, the thickness of rafted ice does not decrease even under influences of divergent sea ice motions. On the other hand, rafting of young ice such as grease ice does not contribute to increase in sea ice thickness, because grease ice behaves like a fluid. In order to take into account such non fluid-like sea ice properties, rafting of grease ice is ignored in this study using a proxy of sea ice type called as "Gradient Ratio (*GR*). *GR* was introduced by Cavalieri et al. (1984) by the following equation,

$$GR_{(a/b)V} = \{T_a(V) - T_b(V)\}/\{T_a(V) + T_b(V)\}, \quad (3.3.2)$$

where $T_a(V)$ and $T_b(V)$ are brightness temperatures of the vertical polarized frequencies *a* and *b*. Although *GR* does not identify actual sea ice thickness, *GR* distinguishes old ice from young ice by difference of their surface salinity (Comiso et al., 1997). Then, we empirically set the threshold of *GR* (GR_T), and rafting of sea ice with $GR \geq GR_T$ is set to zero. Krishfield et al. (2014) adopted $GR_{(36/06)V}$ =-0.025 as the threshold between MYI and FYI. In the AMSR-E period, the maximum value of the averaged $GR_{(36/06)V}$ during November to April was about zero (not shown). Then, we set three thresholds in the range of $-0.025 < GR_{(36/06)V} < 0$ as listed in Table 4.

With these assumptions, R is calculated by

$$R(\vec{r},t) = \begin{cases} 0, & A_F(\vec{r},t) \leq 100\%, \\ (A_F(\vec{r},t) - 100)\,\%, & A_F(\vec{r},t) > 100\%, \\ & GR(\vec{r},t) \leq GR_T, \end{cases} \qquad (3.3.3)$$

at each position, $\vec{r}$. Values of $R(\vec{r},t)$ and $GR(\vec{r},t)$ are linearly interpolated from values at Eulerian grids. As a first step to evaluate influences of the mechanical sea ice growth during winter on sea ice conditions in the following spring, we assume the integrated values of $R(\vec{r},t)$ along Lagrangian sea ice trajectories from 1 November to 1 May as a proxy of effects of sea ice rafting caused by the convergence of sea ice motions using the following equation,

$$EC(\vec{r},t) = \sum_{t=1} R(\vec{r},t). \quad (3.3.3)$$

Hereafter, the integrated values calculated by Eq. (3.3.3) are called as "effective convergence (EC)".

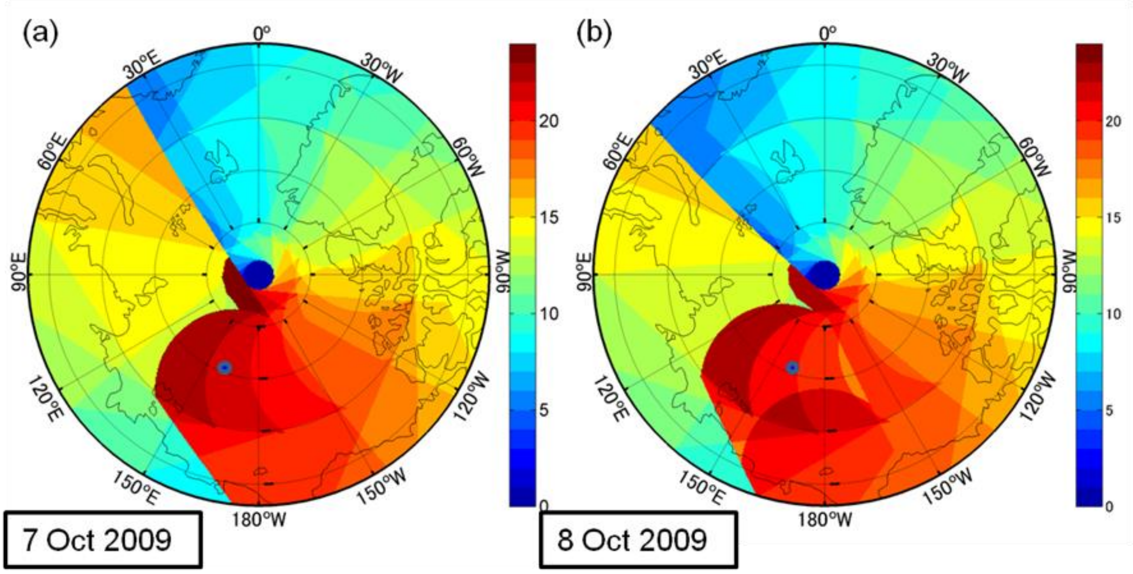

Figure14 Spatial distributions of timings of measurements (*Tm*) of daily-averaged *Tb* and *A* on **a** 7 October 2009 and **b** 8 October 2009.

Table 4 Thresholds of $GR_{(36/06)V}$.

	$GR_T(1)$	$GR_T(2)$	$GR_T(3)$
$GR_{(36/06)V}$	- 0.010	-0.015	-0.020

3.4 Result

3.4.1 Relationship between on the early May and sea ice concentration during July to September

We first focus on the relationship between *EC* on 1 May and sea ice concentration in the following summer of the AMSR-E period. Figure 15 shows spatial distributions of *EC* on 1 May averaged for the AMSR-E period. The values of *EC* calculated by using $GR_T(2)$ and $GR_T(3)$ (Figs. 15b, c) were smaller than that calculated using $GR_T(1)$ (Fig. 15a), due to decreasing sea ice with $GR(\vec{r},t) < GR_T$ after the 2007 summer. In the all cases, sea ice with relatively large values of *EC* zonally distributed in the coastal region in the Pacific sector (the southern Canada Basin, the Chukchi Sea and the East Siberian Sea), known as choke-points of the NSR. This suggests that locations of sea ice with the large *EC* values before the melt onset are important preconditions for whether the choke-point region will be opened or not in summer.

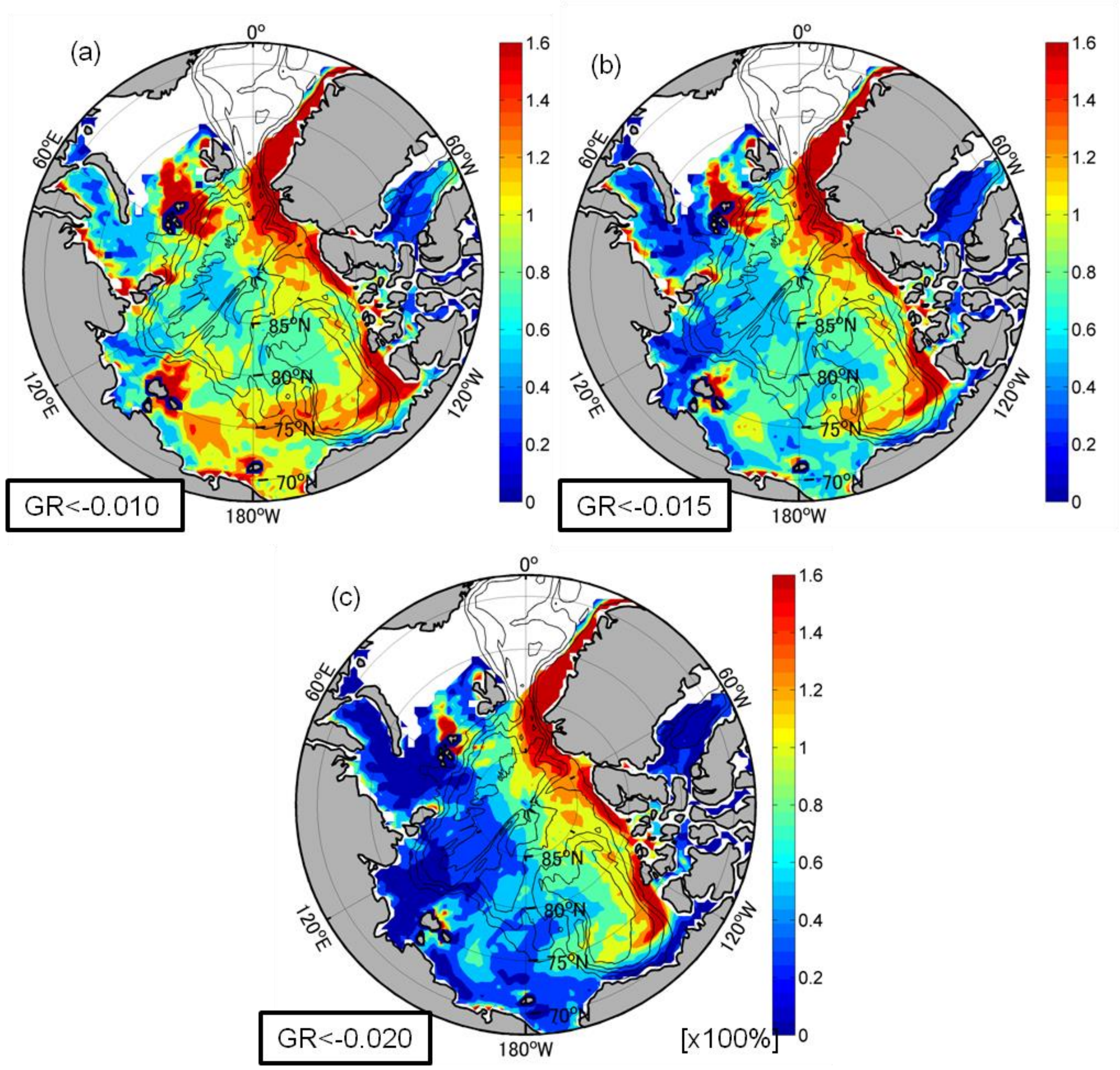

Figure 15 Spatial distributions of *EC* on 1 May, averaged for the AMSR-E period. The values of *EC* were calculated by Eq. (3.3.3) using **a** $GR_T(1)$, **b** $GR_T(2)$, **c** $GR_T(3)$.

Next, we examine predictability of the summer sea ice condition by using only *EC* several months ahead of summer. For planning schedules of the shipping using the NSR, to predict the length of the period, in which the NSR is available, is more important information than to predict the annual minimum values of SIA in the end of summer. In the NSR region, the sea ice cover starts to retreat in July, and the open water area starts to freeze in the late September. Thus, we examine the relationship between *EC* on 1 May and sea ice concentration averaged during July to September. Here, we use values of *EC* on 1 May calculated using $GR_T(3)$. In fact, in the choke point regions in the Pacific sector, *EC* on 1 May and the summer (July-September) sea ice concentration are correlated with each other with a correlation coefficient >0.58, which is significant at 90 % confidence level (the area enclosed by green contours in Fig. 16). This suggests that variations of summer sea ice concentration in the coke-point regions can be estimated several months ahead of summer using only satellite-derived data.

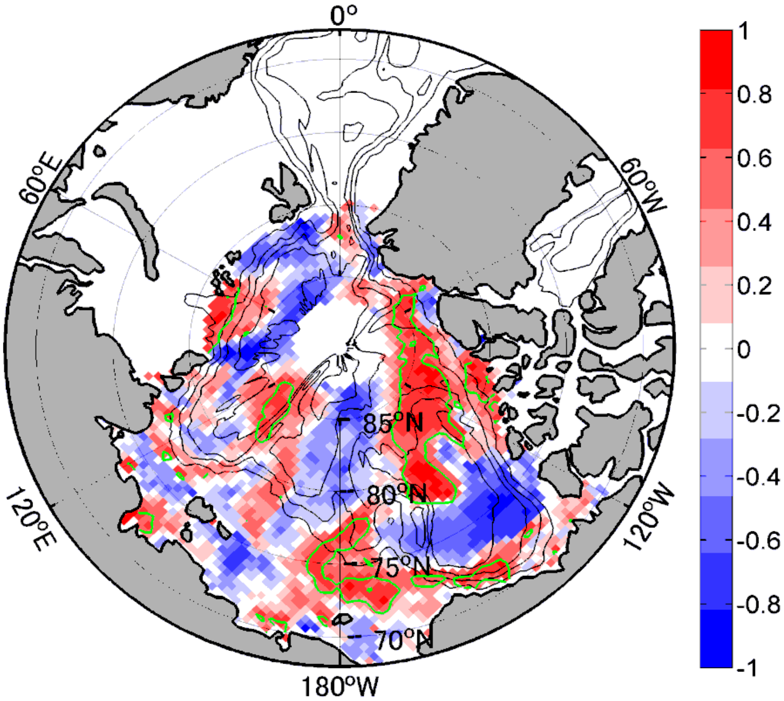

Figure 16 Correlation coefficients between *EC* on 1 May and sea ice concentration averaged during July to September of the AMSR-E period. The values of *EC* was calculated by Eq. (3.3.3) with $GR_T(3)$. The *green contour* encloses regions of > 90% confidence level for the two-tailed *t* test.

3.4.2 Sea ice conditions in 2015

In the choke-point region, the zonal ice band was observed in the mid-summer of 2015 (Fig. 12b). Taking the sea ice condition in 2015 as an example, we check the validity of our estimation of effects of sea ice rafting. Figures 17a and 17b show spatial distributions of *EC* on 1 May 2015 and of the observed sea ice concentration in August 2015, respectively. In the early May, sea ice with relatively large *EC* zonally distributed in the area from the southern Canada Basin to the Chukchi Sea and southwest of the

Wrangel Island (Fig. 17a). Three months later, the zonal distribution of sea ice concentration was also found over these regions, but its location shifted slightly northward especially in the Chukchi Sea, suggesting influences of the sea ice drifting caused by winds during May to July (Fig. 17b). Although a consideration of sea ice movements is required for a better prediction of the sea ice retreat, similar spatial patterns between *EC* in the early May and the observed sea ice concentration in the following August suggest that summer sea ice variations in the choke-point regions in the 2015 summer were preconditioned by relatively large *EC* in the preceding spring.

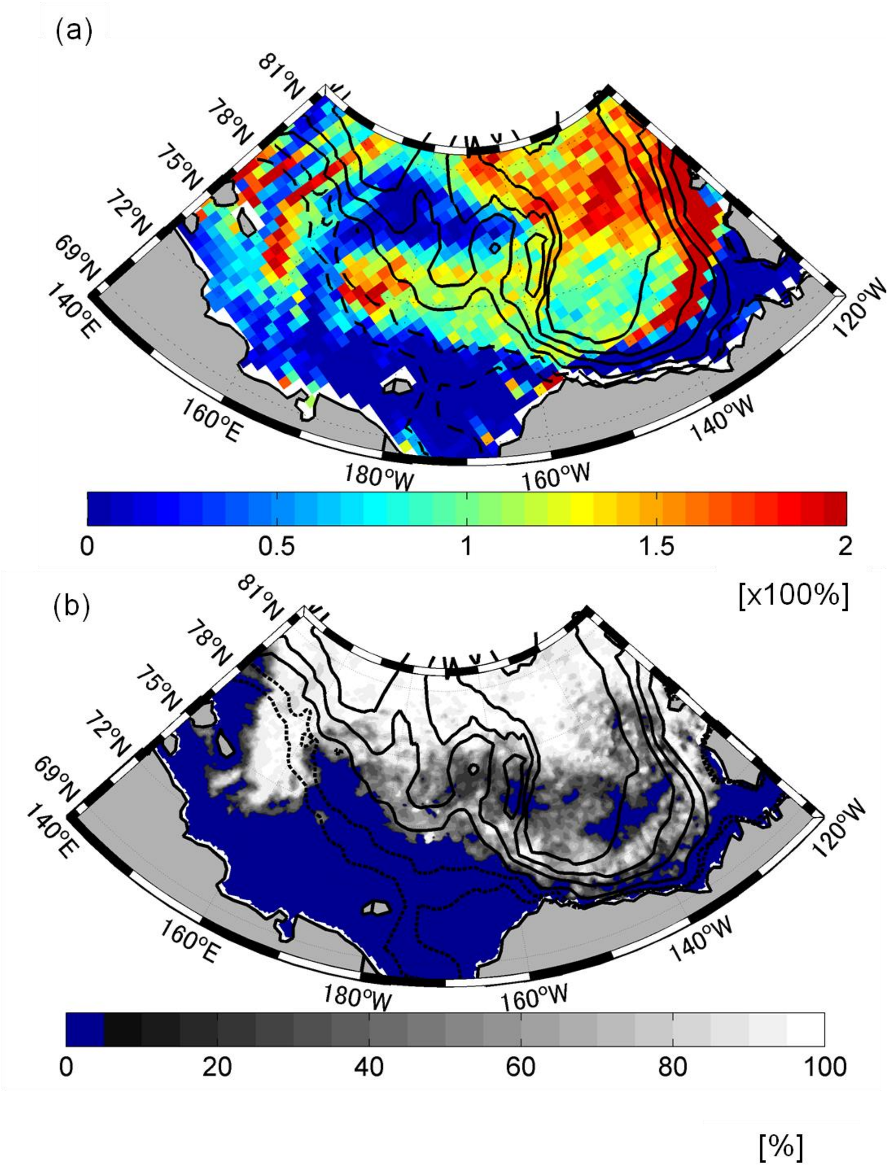

Figure 17 Spatial distributions of **a** *EC* on 1 May 2015 and **b** the observed sea ice concentration [%] in August 2015.

3.5 Summary

In the Arctic coastal regions utilized as the NSR, the dominant sea ice type was displaced from MYI by FYI after the anomalous sea ice reduction in the 2007 summer. In the FYI dominant situation, the sea ice thickness in spring, which is an important precondition of summer sea ice distributions, mainly depends on sea ice growth in the preceding winter. In this section, we estimated effects of sea ice rafting caused by convergent sea ice motions, which contributes to mechanical sea ice growth, using satellite-derived data. Here, we assumed that sea ice rafting was caused by convergent sea ice motions when the following two conditions were satisfied: (1) $A_F > 100\%$, (2) $GR(\vec{r}, t) \leq GR_T$. Then, we also assumed the integrated values of $R = (A_F - 100)$ % along Lagrangian sea ice trajectories as a proxy of sea ice rafting ("effective convergence [*EC*]").

The values of *EC* in the early May, just before the melt onset, were relatively large in the choke-point regions in the Pacific sector of the Arctic Ocean such as the southern Canada Basin, the Chukchi Sea, and the East Siberian Sea. In these regions, the values of the correlation coefficient between *EC* in the early May and the observed sea ice concentration averaged during July to September were high at 90% confidence level. This suggests the predictability of summer sea ice conditions in these regions using only satellite-derived data.

4 General conclusions

In the prediction of sea ice distributions, the spring sea ice thickness is critical to sea ice variations in the following summer. Since the dominant sea ice type in the Arctic Ocean has been displaced from MYI by FYI during the last decade, sea ice growth during winter mainly affects the sea ice thickness in the following spring. In the present study, the methods to estimate two key factors affecting winter sea ice growth thermodynamically and mechanically were developed using satellite-derived data.

Using in-situ hydrographic data from the late 1990s to the mid-2000s, the previous study qualitatively demonstrated that the increased subsurface oceanic heat transport originating in the warm PSW led less sea ice formations during winter and resultant sea ice reductions in the following summer (Shimada et al., 2006). In order to quantify influences of oceanic heats on summer sea ice variations, the volume transport of the upper ocean circulation that transported PSW from the shelf region to the basin was estimated, with a particular focus on the period after the mid-2000s.

To develop the estimation method, temporal variations of observed parameters (winds, sea ice motions, the volume transport of the upper ocean circulation and SIA) were examined. The temporal variations of the volume transport that was an indicator of the thermal state in the upper ocean showed the time lag relative to that of the surface forcing. The evaluated time scale of this delayed oceanic response relative to the surface forcing in 2006-2012 was about three years. This quantitative result allowed us to estimate the temporal variations of the volume transport with high accuracies using only satellite-derived sea ice motion data.

The temporal variations of the PSW temperature (color in Fig. 8) in the Northwind Ridge area additionally delayed about two years relative to that of the volume transport of the OBG (Fig. 6c). For example, the maximum volume transport was observed in 2010, whereas the maximum temperature of PSW in the Northwind Ridge area was observed in 2012. Since PSW is usually entrained around the Barrow Canyon into the upper ocean circulation and then is carried onto the Northwind Ridge area, it is expected that the advective time of PSW is associated with the time lag between the volume transport and the PSW temperature in the Northwind Ridge area. For example, the mean advective velocity from the Barrow Canyon to the Northwind Ridge area was estimated to be about 1.7 cm s^{-1}, using the observed ODH distribution at 100 dbar in 2011 (center panel in third line of Fig. 7). The estimated advective time of about two years roughly corresponds to the observed time lag between the temporal variations of the volume transport and that of the PSW temperature in the basin. When the underlying PSW was warmest in 2012 (color in Fig. 8), the record minimum of the summer SIA was observed (Fig. 6d). The above coupled variations between ocean and sea ice enable us to predict influences of subsurface ocean heats on summer sea ice variations within the time scale of the delayed oceanic response.

On the other hand, sea ice rafting caused by convergent sea ice motions is another key factor affecting winter sea ice growth mechanically. In this study, using satellite-derived data, we calculated the temporal variations of sea ice concentration influenced by the convergence of sea ice motions (A_F), and assumed that the integrated values of $(A_F - 100)$ % along Lagrangian sea ice trajectories as a proxy of effects of sea ice rafting (*EC*). The values of *EC* in the early May were large in the choke-point regions of the NSR in the Pacific sector of the Arctic Ocean. The values of the correlation coefficient between *EC* in the early May and the observed sea ice concentration averaged during July to September were high (r>0.58) in the choke-point regions, suggesting the predictability of the summer sea ice variations in these regions by using only satellite-derived data several months ahead of summer.

In the above estimation of mechanical sea ice growth, we assumed that influences of thermodynamic sea ice growth were uniform everywhere in the Arctic Ocean. However, the increase in the horizontal ocean heat transport due to the strengthening of the OBG pointed out in Sect. 2 suggests that the thermodynamic sea ice growth in the Northwind Ridge area would be smaller than that in regions in which the warm PSW did not influence the thermal state of the upper ocean. Additionally, in the Pacific sector of the Arctic Ocean, sea ice with large sea ice rafting was often found in the early May. Therefore, prediction models constructed using two estimation method presented in this study would provide better predictions of summer sea ice variations in these regions.

In the present study, we estimated ocean stratifications with the assumption that the vertical heat diffusivity was constant, and this assumption would be appropriate for the prediction of the thermal state of the upper ocean in the most of cases. Exceptionally, the cooling in the subsurface PSW layer in the Northwind Ridge area was found during 2007 to 2008, suggesting an event-like upward heat release (color in Fig. 8). In the Atlantic sector of the Arctic Ocean, the warm Atlantic Water (AW) is also delivered into the Arctic Ocean. Since its intermediate depth is deeper than about 150m, it is expected that the AW does not affect the sea ice formation in the surface mixed layer. However, Polyakov et al. (2013) reported that upward heat fluxes from the AW layer to the surface mixed layer were caused by the strong convections due to weakened ocean stratifications in recent years. They estimated that the observed upward heat flux originating in AW corresponded to sea ice loss of ~0.10 m/year. Therefore, by taking into account abrupt vertical heat fluxes due to weakened stratifications, the estimation method of the thermal state of the upper ocean affecting sea ice formations would be improved so that it can predict event-like anomalous reduction of the sea ice cover.

Appendix

Appendix A　Propagation of planetary and topographic Rossby waves

The observational evidence showed that the sea ice motion with an annual frequency has been dominant in the Canada Basin (Fig. A1). In the Canada Basin, the baroclinic planetary Rossby wave with this dominant frequency cannot freely propagate due to small β effects (Sumata and Shinada 2007). They also pointed out that the topographic β effect is also too small in the central Canada Basin with flat seafloor topographies to induce baroclinic topographic Rossby waves with the annual frequency. However, there are gradual zonal slopes in the southeastern Canada Basin (white contours in Fig. A2). Figure A2 shows the spatial distribution of the maximum frequency of the baroclinic topographic Rossby wave calculated in the following equation,

$$\sigma_{\mathrm{max}\_topgraphy(bl)} = -\frac{F_1}{F_1+F_2}\frac{\alpha}{2\sqrt{l^2+F_1+F_2}}, \text{(A1)}$$

$$F_1 = f_0^2 / g'H_1,\ \ F_2 = f_0^2 / g'H_2,$$

$$f_0 = 2\Omega \sin\theta,\ \ g' = (\rho_1/\rho_2)g,$$

in the case that the hydrographic structure in the Canada Basin assumed as the linearized two-layer ocean. g' is a reduced gravity with densities of the upper and lower layers, ρ_1 and ρ_2. α is a zonal gradient of bottom topographies. l is a zonal width of the Canada Basin. Here, parameters listed in Table A1 are substituted in Eq. (A1). In the southeastern portion of the Canada Basin, disturbances induced by the surface forcing with the annual frequency can be emanated as baroclinic topographic Rossby waves (Fig. A2). This suggests that the surface forcing imposed on the sea surface in this region does not contribute to formations of spatial patterns of the OBG. Thus, the wind and sea ice velocity curls in the southeastern portion of the Canada Basin did not used for the reconstruction of ODH$_{center}$, and we set the zonal band depicted in Fig. A2 (same as the zonal band depicted in Fig. 4), in which both curls were averaged.

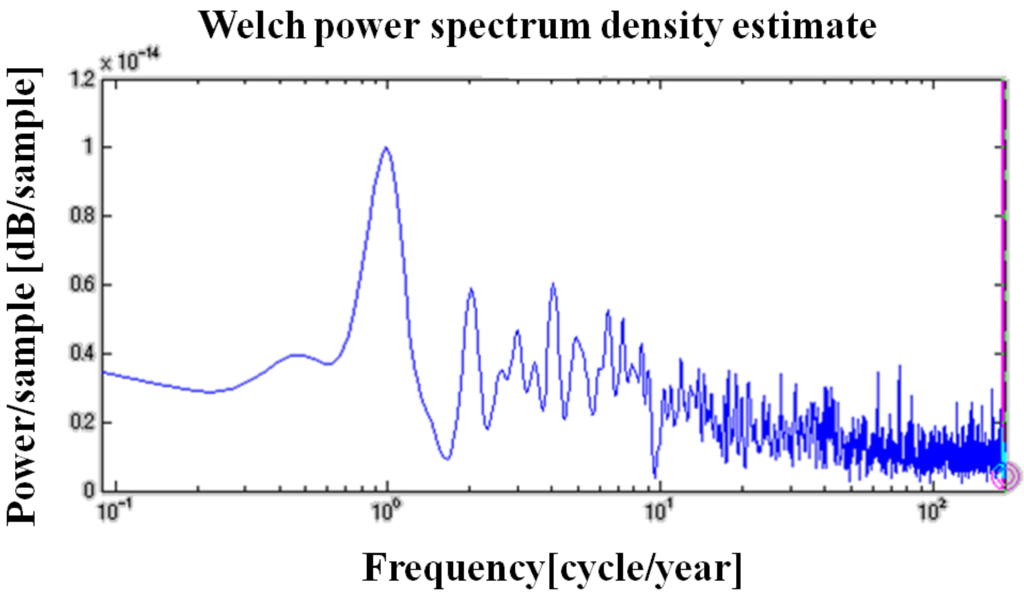

Figure A1 Welch power spectrum density estimate of the sea ice velocity curl $[s^{-1}]$ at the location of 81.3°N and 167.0°W calculated using satellite-derived sea ice motion velocities during January 1991 to March 2011.

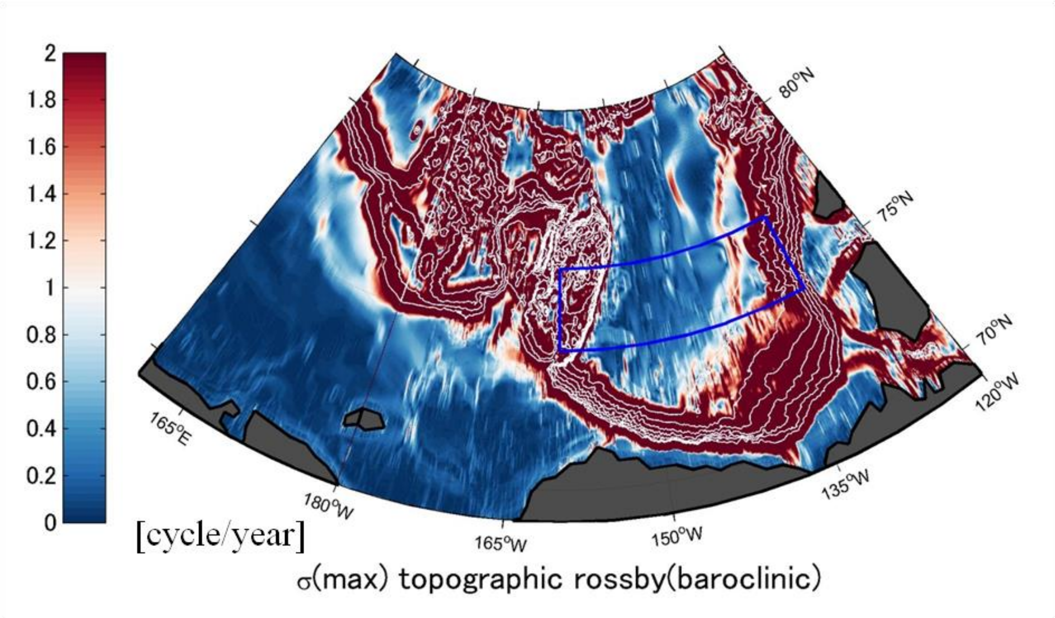

Figure A2 Spatial distributions of maximum frequencies of baloclinic topographic Rossby waves calculated by Eq. (A1).

Table A1. Parameters substituted to Eq. (A1).

zonal width of the Canada Basin, l=1000 [km]
height of lower layer, $H_1 =$ 3400 [m]
height of upper layer, $H_2 =$ 200 [m]
Earth's angular velocity, Ω =7.2910^{-5} [rad/s]
Mean latitude of the Canada Basin, θ =75$^{\mathrm{o}}$N
density of lower layer, $\rho_1 = 1028$ [kg m^{-3}]
density of lower layer, $\rho_2 = 1026$ [kg m^{-3}]

Appendix B Properties of sea ice motions

In Sect. 2.4.1, the time series of the sea ice velocity curl shown in Fig. 6b showed the step-function like changes with abrupt decreases in SIA in 1989, 1998 and 2007, even though the wind curl showed the oscillatory variation (Fig. 6a), suggesting changes in properties of sea ice motion relative to wind forcing. In recent years, several studies showed that the enhanced sea ice motion observed after the mid-2000s did not caused by the increase in wind speed, and speculated that the increased sea ice motion was associated with the thinning of the Arctic ice cover (Rampal et al., 2009; Spreen et al., 2011; Kwok et al., 2013). Using a proxy of the kinematic coupling between atmosphere and sea ice, we briefly review changes in the property of the response of sea ice motion relative to the wind forcing in 1988-1997 (Period 1), 1998-2006 (Period 2) and 2007-2012 (Period 3), with a particular focus on sea ice motions in the Pacific sector of the Arctic Ocean.

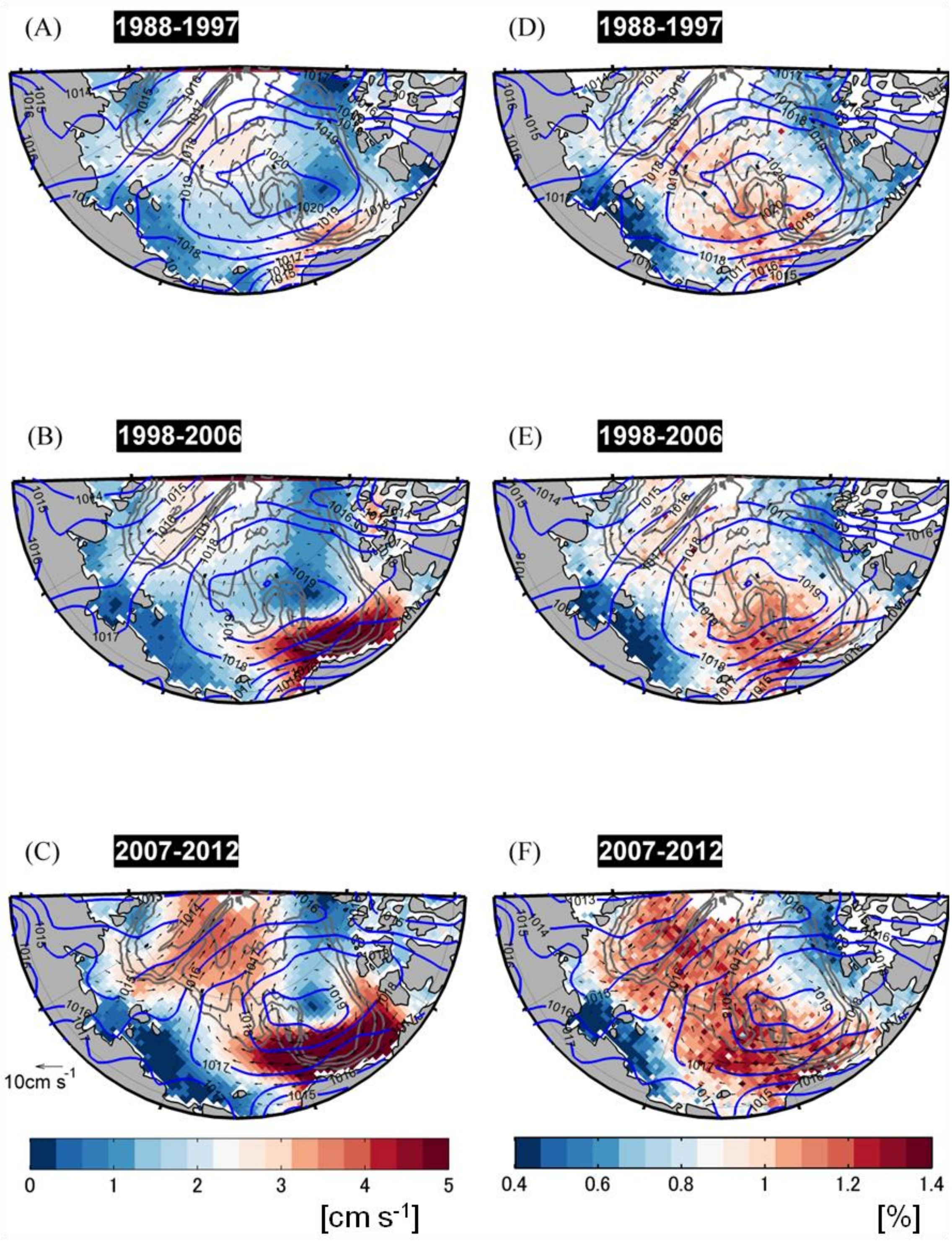

Figure B1 Spatial distributions of absolute sea ice velocity (cm s^{-1}, *color*) in **a** 1988-1997 **b** 1998-2007 **c** 2008-2012, and of WF (*color*) in **d** 1988-1997 **e** 1998-2007 **f** 2008-2012, with SLP (*blue contour*) and sea ice velocity vectors (*vector*) in the ice-covered period (November-June).

Kimura and Wakatsuchi (2000) introduced the ratio of the sea ice velocities, which were tangential to wind vectors, to the wind velocities, as an indicator of changes in response of sea ice motion relative to wind forcing. Hereafter, this ratio is called as a Wind Factor (WF). Before examining changes in WF, we show spatial patterns of the absolute sea ice velocity averaged during the ice-covered period (November-June) in the three periods (color in Figs. B1a-c), with those of SLP (contours). After the late 1990s, the absolute velocity of sea ice increased in the southern Canada Basin and the TDS region (color in Figs. B1 b, c) compared with that prior to the late 1990s (color in Fig. B1a), without changes in the wind strength (contour). In these regions, the values of WF in Period 3 (Fig. B1f) were almost doubled from the values in Period 1 (Fig. B1 d). This suggests that the wind forcing was not a main cause in the increase in WF in recent years.

Figures B2 a-c show spatial patterns of $GR_{(36/18)V}$ averaged during November to April in Period 1, Period 2 and Period3. Blue and red colors represent roughly MYI and FYI, respectively. During Period 1, the most of the Arctic Ocean was covered by thick MYI, except the southern rim of the Canada Basin and the Laptev Sea (Fig. B2a). During Period 2, MYI was replaced by FYI in the Chukchi Sea (Fig. B2b). During Period 3, the MYI coverage decreased not only in the above coastal regions but also in the western half of the Canada Basin and the TDS region instead of the increase in the FYI coverage (Fig. B2c). This suggests that the decrease in the MYI coverage related to the increases in WF as speculated by the previous studies (Rampal et al., 2009; Spreen et al., 2011; Kwok et al., 2013).

Furthermore, inputs of the negative the sea ice velocity curl (Figs. B2e, f) increased in the southern half of the Canada Basin where the dominant sea ice type was changed from MYI to FYI in Period 2 and Period 3 (Figs. B1b, c). Especially, the negative sea ice velocity curl increased in the central Canada Basin where baroclinic topographic Rossby waves cannot propagate (see Appendix A). Thus, this anomalous negative vorticity input from sea ice to the upper ocean would effectively reinforce the OBG in these periods.

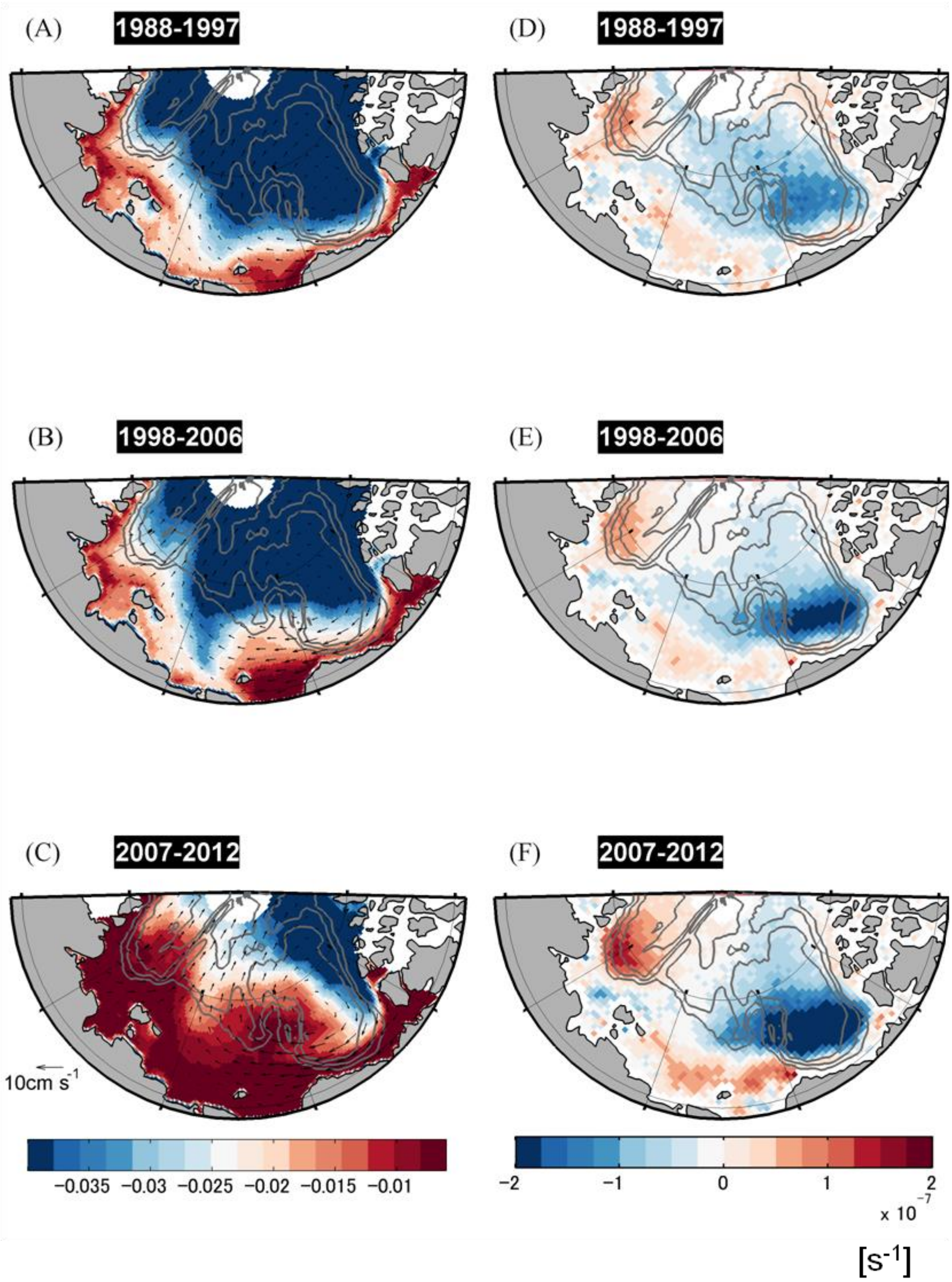

Figure B2 Spatial distributions of **a-c** $GR_{(36/18)V}$ (*color*) with sea ice velocity vectors (*vector*) averaged in November-April of **a** 1988-1997 **b** 1998-2007 **c** 2008-2012, and of the curl of sea ice velocities (*color*) averaged in November-June of **d** 1988-1997 **e** 1998-2007 **f** 2008-2012.

Finally, we argue seasonal variations of the zonally averaged curls. Figure B3 shows time series of anomalies of monthly sea ice velocity curls averaged in the zonal band depicted in Fig. A2. Here, three-month running mean values of normalized curls are used. Through the period from 1978 to 2012, the values of the monthly curls in the Canada Basin were mostly negative (not shown), and thus the positive values of normalized curls in Fig. B3 does not mean anti-clockwise sea ice motion but mean weakened clockwise sea ice motions. The clockwise sea ice motions in the Canada Basin were significantly enhanced after the mid-2000s especially in the early winter (October-December). It is also interesting to note that the extreme negative values are found around June after the late 2000s.

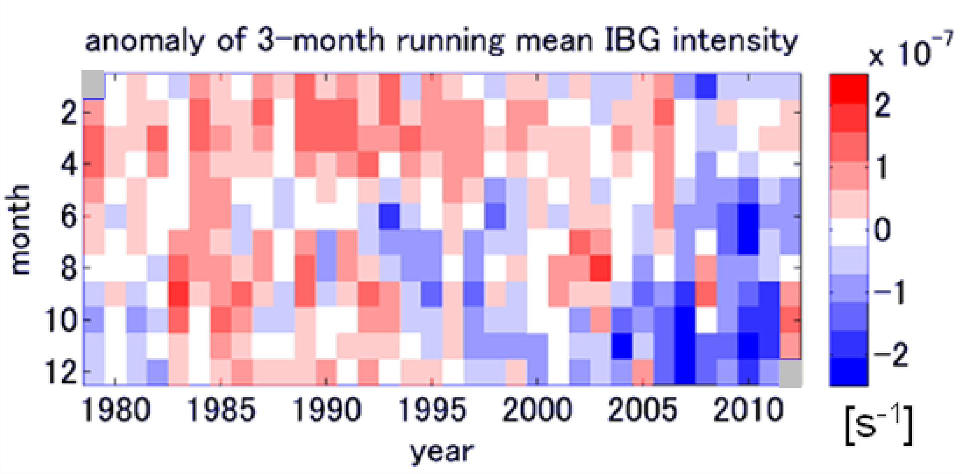

Figure B3 Anomalies of monthly mean of normalized sea ice velocity curls [s^{-1}] averaged in the zonal band depicted in Fig. A2. The three-months running mean values are shown.

Figure B4 shows time series of monthly curls of sea ice velocities averaged for 1978-2007 (dashed curve) and for 2008-2011 (solid curve). In this figure, the values of the "not normalized" sea ice velocity curl averaged in the zonal band in Fig. A2 are used. In both periods, the local maximum of negative curls are found in June and October-November. The clockwise sea ice motions were enhanced in the early winter in the latter period compared that in the former period, suggesting that the seasonally amplified surface forcing would contribute to the drastic enhancement of the OBG after 2007.

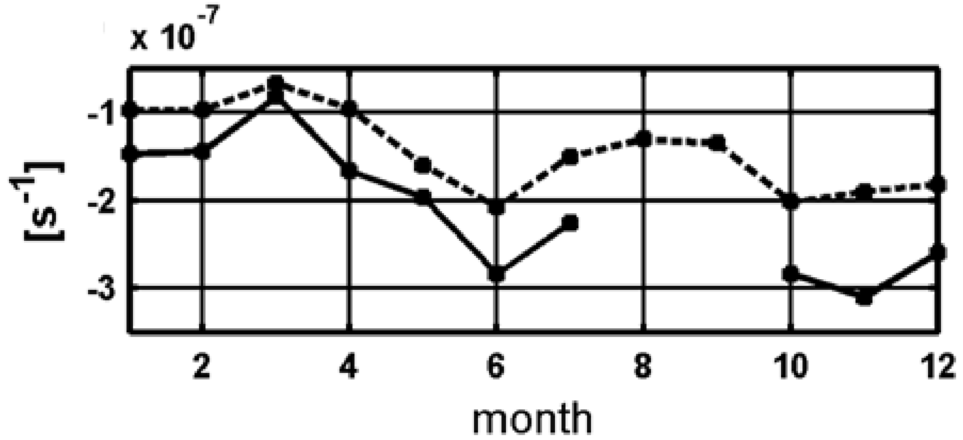

Figure B4 Time series of monthly averages of the sea ice velocity curls [s^{-1}] in the *zonal band* depicted in Fig. A2 for 1978-2007 (*dashed curve*) and for 2008-2012 (*solid curve*). The values of the sea ice velocity curl averaged in the case that the observed sea ice concentration in the zonal band was more than 80% were plotted.

Appendix C Verifications for sea ice trajectories

To validate the performance of the calculated sea ice trajectories by using satellite-derived sea ice motion data described in Sect. 3.3.3, locations of the Ice-tethered profiler (ITP) buoy detected by GPS are used here. A backward position of sea ice $\vec{r}$ is given by

$$\vec{r}(t) = \vec{r}(t) - \Delta t \times \vec{u}(\vec{r}, t + \frac{\Delta t}{2}) \quad \text{(C1).}$$

Since timings of measurements of sea ice velocities also differ from region to region as shown in Fig. 14, a time interval Δt is not a constant value. Figure C1 shows temporal variations of Δt used in Eq. (C1) along the Lagrangian trajectory of ITP 8 obtained from the GPS observation during November 2008 to April 2009. The mean values of Δt in the period was about 24 hours, however, Δt was fluctuated from 5 hours to 35 hours. Therefore, Δt depending of the difference of timings of measurements at $\vec{r}(t)$

and $\vec{r}(t+\Delta t)$ is used in this study.

For the verification of the estimated Lagrangian backward trajectories, we tracked position of ITP8 backward from 1 May 2009 to 1 November 2007. During this period, the ITP8 buoy drifted in the Canada Basin. Distances between the observed and estimated positions are shown in Fig. C2. From April 2009 to November 2008, the distances between the estimated and observed backward positions were less than 40 km. The distances, however, started to increase when backward positions were estimated from summer sea ice motion data and reached about 100 km that is more than twice of the pixel size of sea ice velocity data. These increased errors in summer would be resulted from that the accuracies of satellite-derived sea ice velocities in May-October (the root mean square *D*=3.4 cm s^{-1}) was larger than that in November-April (*D*=2.5 cm s^{-1}). Same features of the estimation error of Lagrangian trajectories were found in the cases using data from ITP 11, 13 and 35 that also drifted in the Canada Basin (not shown). Thus, we estimate mechanical sea ice growth along Lagrangian backward trajectories of sea ice calculated using sea ice velocity data during November to April with higher accuracies than the sea ice velocity during May to October.

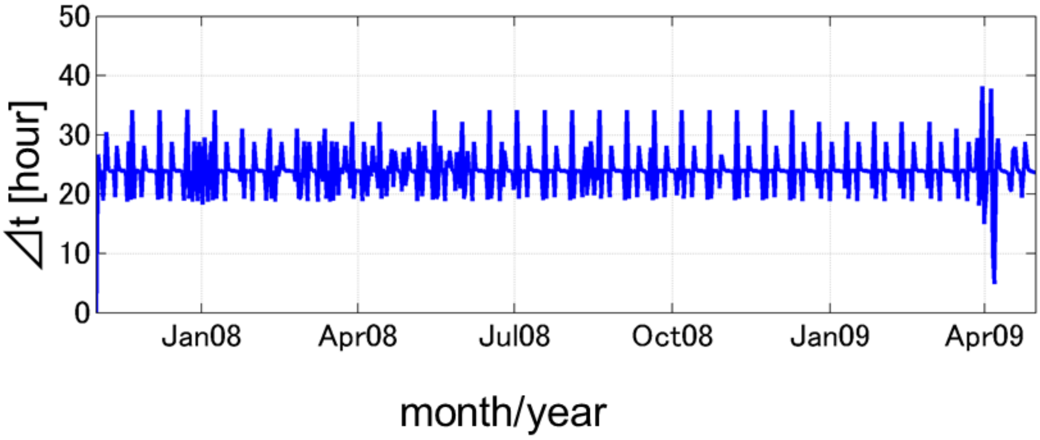

Figure C1 Temporal variations of Δt [hours] along the Lagrangian trajectory of ITP 8 obtained from the GPS observation during November 2008 to April 2009

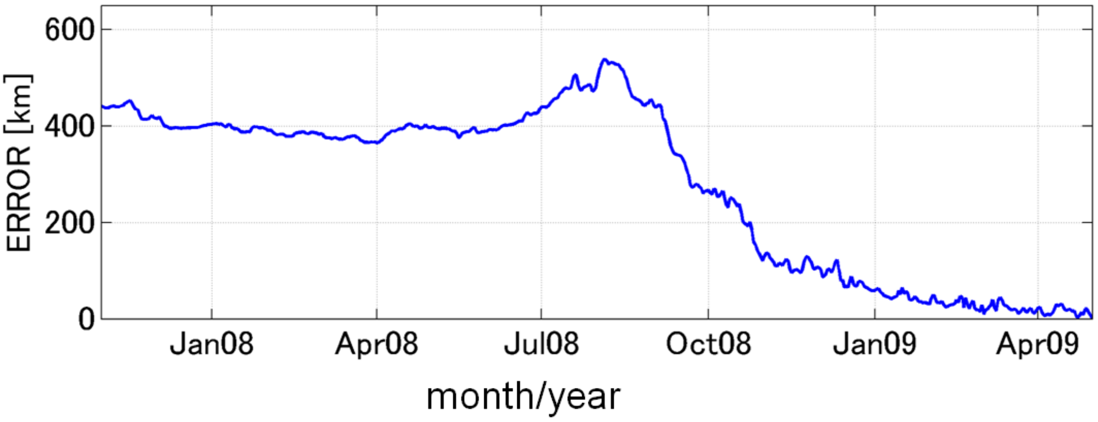

Figure C2 Time series of the distance [km] between the observed and estimated positions of ITP8 from 1 May 2009 to 1 November 2007.

Figure C3 shows Lagrangian backward sea ice trajectories that were tracked backward from 1 May to 1 November of the preceding year in the AMSR-E period with the mean sea ice motion fields. These trajectories indicate large spatial variabilities of sea ice motions. For example, sea ice traveled several hundred km in the southern Canada Basin along the Alaskan coast, whereas those in the northern Canada Basin were stagnated during the 2007/2008 winter (Fig. C3f). The spatial distributions of sea ice trajectories also show that there were large inter-annual variabilities of the sea ice motion fields. For example, sea ice motion was stagnated in the most Arctic Ocean during the 2005/2006 winter (Fig. C3d), whereas sea ice traveled longer distances during the 2007/2008 winter (Fig. C3f).

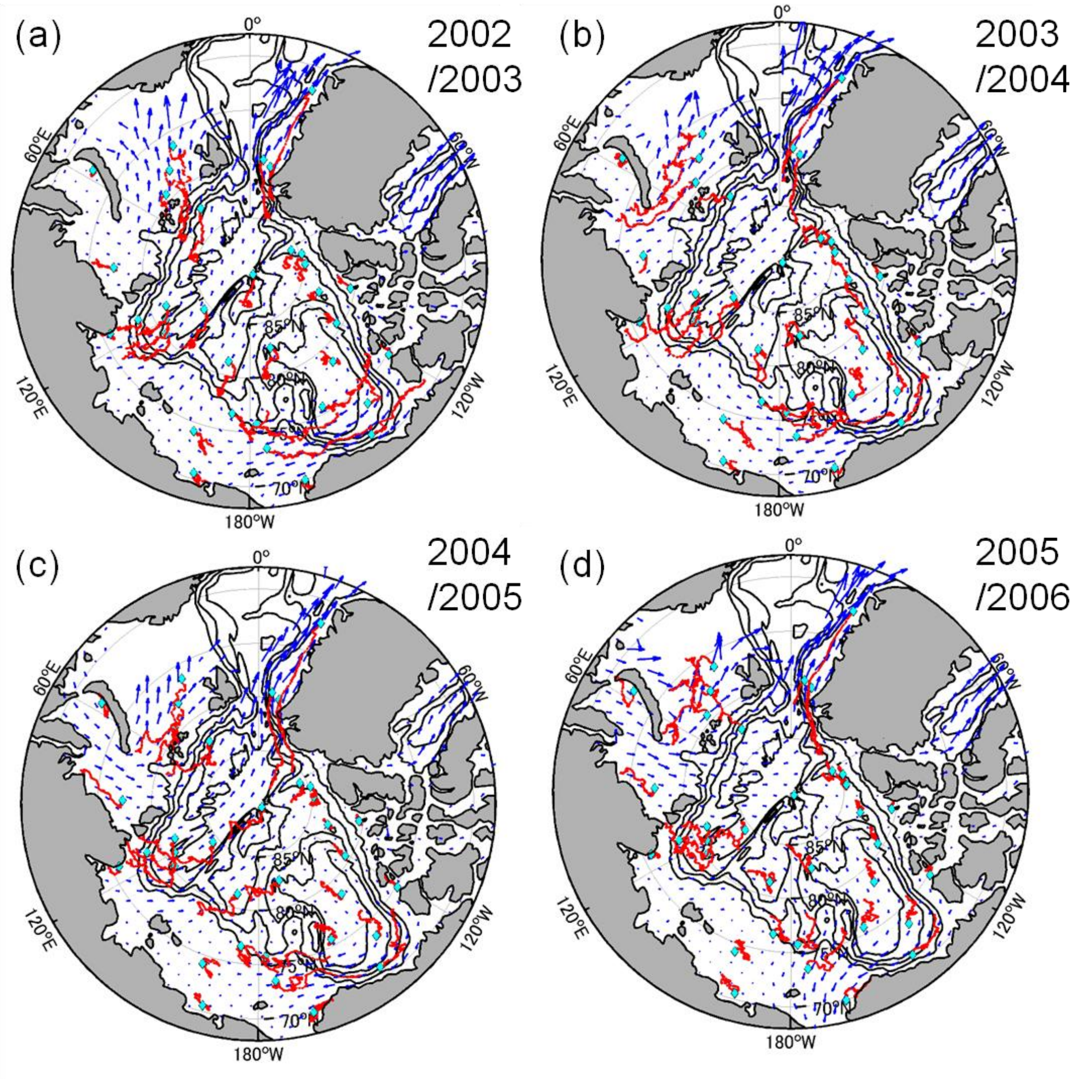
(a)
2002
/2003
(b)
2003
/2004
(c)
2004
/2005
(d)
2005
/2006
0°
60°E
120°E
180°W
120°W
60°W
85°N
80°N
75°N
70°N

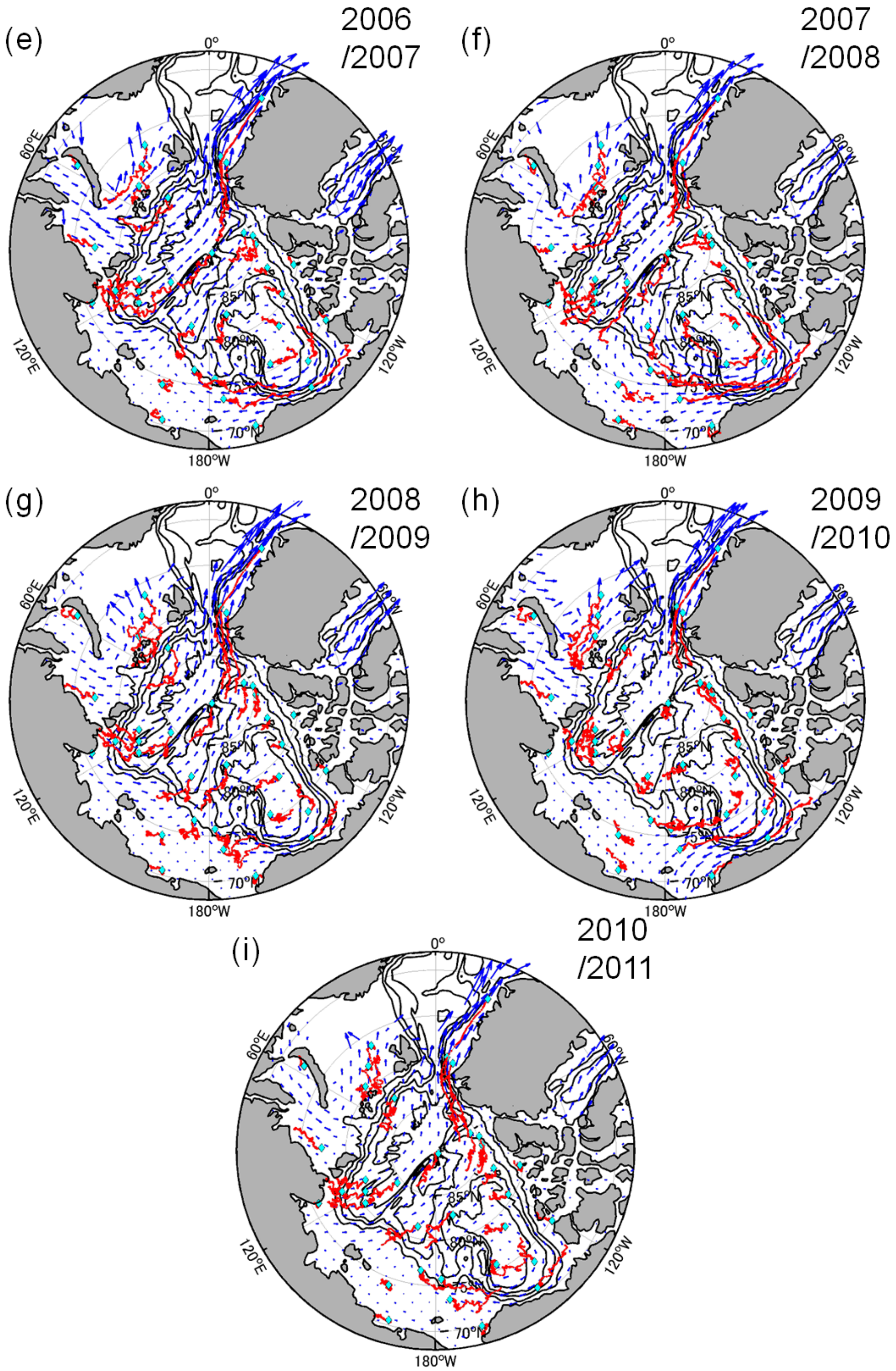

FigureC3 Spatial distributions of Lagrangian sea ice trajectories tracked backward from 1 May to 1 November of the preceding year (*red contours*) and mean sea ice vectors in winter (November-April) (*blue vectors*). Cyan dots represent positions of sea ice at 1 May of each year.

Reference

Adrian, R. J. (1991), Particle imaging techniques for experimental fluid mechanics. *Ann Rev Fluid Mech* 23 261 (304)

Cavalieri, D. J., C. L. Parkinson, P. Gloersen, and H. J. Zwally (1996), updated yearly. *Sea Ice Concentrations from Nimbus-7 SMMR and DMSP SSM/I-SSMIS Passive Microwave Data, Version 1*. [indicate subset used]. Boulder, Colorado USA. NASA National Snow and Ice Data Center Distributed Active Archive Center. http://dx.doi.org/10.5067/8GQ8LZQVL0VL.

Cavalieri D. J., P. Gloersen, and W. J. Campbell (1984), Determination of sea ice parameters with the NIMBUS 7 SMMR. *J. Geophys. Res*.89(D4) 5355–5369

Comiso, J. C. (2011), Large Decadal Decline of the Arctic Multiyear Ice Cover. *J. Clim* 25 30688 1176–1193. doi: http://dx.doi.org/10.1175/JCLI-D-11-00113.1

Comiso, J. C., C. L. Parkinson, R. Gersten, and L. Stock (2008), Accelerated decline in the Arctic sea ice cover, *Geophys. Res. Lett.*, 35, L01703, doi:10.1029/2007GL031972

Comiso, J. C., D. J. Cavalieri, C. L. Parkinson, and P. Gloersen (1997), “Passive microwave algorithms for sea ice concentration: A comparison of two techniques,” *Remote Sens. Environ.*, vol. 60, no. 3, pp. 357–384, Jun

Francis, J. A., W. Chan, D. J. Leathers, J. R. Miller, and D. E. Veron (2009), Winter Northern Hemisphere weather patterns remember summer Arctic sea-ice extent, *Geophys. Res. Lett.*, 36, L07503, doi:10.1029/2009GL037274

Honda, M., J. Inoue, and S. Yamane (2009), Influence of low Arctic sea-ice minima on anomalously cold Eurasian winters, *Geophys. Res. Lett.*, 36, L08707, doi:10.1029/2008GL037079

Holland, M. M., C. M. Bitz, and B. Tremblay (2006), Future abrupt reductions in the summer Arctic sea ice, *Geophys. Res. Lett.*, 33, L23503, doi:10.1029/2006GL028024

Jones, R.N., A. Patwardhan, S.J. Cohen, S. Dessai, A. Lammel, R.J. Lempert, M.M.Q. Mirza, and H. von Storch (2014), Foundations for decision making. In: *Climate Change 2014: Impacts, Adaptation, and Vulnerability. Part A: Global and Sectoral Aspects. Contribution of Working Group II to the Fifth Assessment Report of the Intergovernmental Panel on Climate Change* [Field, C.B., V.R. Barros, D.J. Dokken, K.J. Mach, M.D. Mastrandrea, T.E. Bilir, M. Chatterjee, K.L. Ebi, Y.O. Estrada, R.C. Genova, B. Girma, E.S. Kissel, A.N. Levy, S. MacCracken, P.R. Mastrandrea, and L.L. White (eds.)]. Cambridge University Press, Cambridge, United Kingdom and New York, NY, USA, pp. 195-228

Kalnay, E., M. Kanamitsu, R. Kistler, W. Collins, D. Deaven, L. Gandin, M. Iredell, S. Saha, G. White, J. Woollen, Y. Zhu, A. Leetmaa, R. Reynolds, M. Chelliah, W. Ebisuzaki, W. Higgins, J. Janowiak, K. C. Mo, C. Ropelewski, J. Wang, Roy Jenne, and D. Joseph (1996), The NCEP/NCAR 40-Year Reanalysis Project. *Bull. Amer.*

Meteor. Soc., 77, 437–471.
doi: http://dx.doi.org/10.1175/1520-0477(1996)077<0437:TNYRP>2.0.CO;2

Kamoshida T., and K. Shimada (2010), Long term sea ice motion dataset in the Arctic from SMMR, SSM/I and AMSR-E. *Second International Symposium on the Arctic Research* pp.125

Khon, V. C., I. I. Mokhov, M. Latif, V. A. Semenov, and W. Park (2010), *Perspectives of Northern Sea Route and Northwest Passage in the twenty-first century*. *Clim. Change* 100, 757–768

Kimura, N., A. Nishimura, Y. Tanaka, and H. Yamaguchi (2013), Influence of winter sea-ice motion on summer ice cover in the Arctic. *Polar Research***,** [S.l.], ISSN 1751-8369. Available at:
<http://www.polarresearch.net/index.php/polar/article/view/20193>.

Kimura, N., M. Wakatsuchi (2000), Relationship between sea-ice motion and geostrophic wind in the Northern Hemisphere. *Geophys. Res. Lett*., 27 3735–3738. doi: 10.1029/2000GL011495

Krishfield, R. A., A. Proshutinsky, K. Tateyama, W. J. Williams, E. C. Carmack, F. A. McLaughlin, and M.-L. Timmermans (2014), Deterioration of perennial sea ice in the Beaufort Gyre from 2003 to 2012 and its impact on the oceanic freshwater cycle, *J. Geophys. Res. Oceans,* 119, 1271–1305, doi:10.1002/2013JC008999

Krishfield, R., J. Toole, A. Proshutinsky, and M-L. Timmermans (2008), Automated

Ice-Tethered Profilers for Seawater Observations under Pack Ice in All Seasons. *J. Atmos. Oceanic Technol.*, 25, 2091–2105

Kwok, R., G. Spreen, and S. Pang (2013), Arctic sea ice circulation and drift speed: Decadal trends and ocean currents, *J. Geophys. Res. Oceans*, 118, 2408–2425, doi:10.1002/jgrc.20191

Kwok, R., and J. Morison (2011), Dynamic topography of the ice-covered Arctic Ocean from ICESat. *Geophys. Res. Lett.*, 38 L02501. doi:10.1029/2010GL046063

Kwok, R., G. F. Cunningham (2010), Contribution of melt in the Beaufort Sea to the decline in Arctic multiyear sea ice coverage: 1993–2009. *Geophys. Res. Lett.*, 37 L20501. doi:10.1029/2010GL044678

Kwok, R., D. A. Rothrock (2009), Decline in Arctic sea ice thickness from submarine and ICESat records: 1958–2008. *Geophys. Res. Lett.*, 36 L15501. doi:10.1029/2009GL039035

Markus, T., J. C. Stroeve, and J. Miller (2009), Recent changes in Arctic sea ice melt onset, freezeup, and melt season length. *J. Geophys. Res.*. 114 C12024. doi:10.1029/2009JC005436

Maslanik, J., J. Stroeve, C. Fowler, and W. Emery (2011), Distribution and trends in Arctic sea ice age through spring 2011. *Geophys. Res. Lett.*, 38 L13502. doi:10.1029/2011GL047735

Polyakov, I. V., V. Andre, P, R. Rember, L. Padman, E. C. Carmack, and M. J. Jennifer (2013), Winter Convection Transports Atlantic Water Heat to the Surface Layer in the Eastern Arctic Ocean*. *J. Phys. Oceanogr.*, 43, 2142–2155. doi: http://dx.doi.org/10.1175/JPO-D-12-0169.1

Polyakov, I. V., J. E. Walsh, R. Kwok (2012), Recent Changes of Arctic Multiyear Sea Ice Coverage and the Likely Causes. *Bull Amer Meteor Soc* 93 145–151. doi: http://dx.doi.org/10.1175/BAMS-D-11-00070.1

Proshutinsky, A., R. H. Bourke, F. A. McLaughlin (2002), The role of the Beaufort Gyre in Arctic climate variability: Seasonal to decadal climate scales. *Geophys. Res. Lett.*, 29(23) 2100, doi:10.1029/2002GL015847

Rampal, P., J. Weiss, and D. Marsan (2009), Positive trend in the mean speed and deformation rate of Arctic sea ice, 1979–2007, *J. Geophys. Res.*, 114, C05013, doi:10.1029/2008JC005066

Rigor, I. G., J. M. Wallace, and R. L. Colony (2002), Response of Sea Ice to the Arctic Oscillation. *J. Climate*, 15, 2648–2663. doi: http://dx.doi.org/10.1175/1520-0442(2002)015<2648:ROSITT>2.0.CO;2

Rothrock, D. A., Y. Yu, and G. A. Maykut (1999), Thinning of the arctic sea-ice cover, *Geophys. Res. Lett.*, 26(23), 3469– 3472.

Shimada, K., T. Kamoshida, M. Itoh, S. Nishino, E. Carmack, F. A. McLaughlin, S. Zimmermann, and A. Proshutinsky (2006), Pacific Ocean inflow: Influence on catastrophic reduction of sea ice cover in the Arctic Ocean. *Geophys. Res. Lett*., 33 L08605. doi:10.1029/2005GL025624

Shimada, K., E. Carmack, K. Hatakeyama, T. Takizawa (2001), Varieties of shallow temperature maximum waters in the Western Canadian Basin of the Arctic Ocean. *Geophys. Res. Lett*., Geophys Res Lett 28 3441–3444. doi: 10.1029/2001GL013168

Spreen, G., R. Kwok, and D. Menemenlis (2011), Trends in Arctic sea ice drift and role of wind forcing: 1992–2009, *Geophys. Res. Lett*., 38, L19501, doi:10.1029/2011GL048970

Steele, M., J. Morison, W. Ermold, I. Rigor, M. Ortmeyer, and K. Shimada (2004), Circulation of summer Pacific halocline water in the Arctic Ocean. *J. Geophys. Res*. 109 C02027. doi:10.1029/2003JC002009

Stroeve, J., M. M. Holland, W. Meier, T. Scambos, and M. Serreze (2007), Arctic sea ice decline: Faster than forecast, *Geophys. Res. Lett*., 34, L09501, doi:10.1029/2007GL029703

Sumata, K., K. Shimada (2007), Northward Transport of Pacific Summer Water along the Northwind Ridge in the Western Arctic Ocean. *Journal of Oceanography* 63 pp. 363-378

Thompson, D. W. J., J. M. Wallace (1998), The Arctic Oscillation signature in the wintertime geopotential height and temperature fields. *Geophys. Res. Lett*., 25(9) 1297–1300. doi:10.1029/98GL00950

Thorndike, A.S., D. A. Rothrock, G. A. Maykut, and R. Colony (1975), The thickness distribution of sea ice. *J. Geophys. Res*. 80:4501–4513

Toole, J.M., R.A. Krishfield, M.-L. Timmermans, and A. Proshutinsky (2011), The Ice-Tethered Profiler: *Argo of the Arctic. Oceanography* 24(3):126–135, http://dx.doi.org/10.5670/oceanog.2011.64

Wang, J., J. Zhang, E. Watanabe, M. Ikeda, K. Mizobata, J. E. Walsh, X. Bai, and B. Wu (2009), Is the Dipole Anomaly a major driver to record lows in Arctic summer sea ice extent?, *Geophys. Res. Lett.*, 36, L05706, doi:10.1029/2008GL036706

Watanabe, E., J. Wang, A. Sumi, H. Hasumi (2006), Arctic dipole anomaly and its contribution to sea ice export from the Arctic Ocean in the 20th century. *Geophys. Res. Lett*., 33 L23703. doi:10.1029/2006GL028112

Yamamoto-Kawai, M., F. A McLaughlin, E. C. Carmack, S. Nishino, K. Shimada, and N. Kurita (2009), Surface freshening of the Canada Basin, 2003–2007: River runoff versus sea ice meltwater. *J. Geophys. Res*. 114 C00A05 doi:10.1029/2008JC005000

Yang, J. (2006) The Seasonal Variability of the Arctic Ocean Ekman Transport and Its Role in the Mixed Layer Heat and Salt Fluxes. *J. Climate* 19 5366–5387. doi: http://dx.doi.org/10.1175/JCLI3892.1